Electrochimica Acta 493 (2024) 144360

Contents lists available at ScienceDirect

Electrochimica Acta

journal homepage: www.journals.elsevier.com/electrochimica-acta

A comparison between physics-based Li-ion battery models

Haider Adel Ali Ali [a,b], Luc H.J. Raijmakers [a,*], Kudakwashe Chayambuka [a], Dmitri L. Danilov [a,c], Peter H.L. Notten [a,c], Rüdiger-A. Eichel [a,b]

[a] Forschungszentrum Jülich GmbH, Institute of Energy and Climate Research (IEK-9), Wilhelm-Johnen-Straße, Jülich 52428, Germany
[b] RWTH Aachen University, Institute of Physical Chemistry, Aachen 52074, Germany
[c] Eindhoven University of Technology, Eindhoven 5600MB, The Netherlands

ARTICLE INFO

Keywords:
Battery modeling
Pseudo-two dimensional (P2D)
Reduced-order models
Single particle model (SPM)
Extended single particle model (ESPM)

ABSTRACT

Physics-based electrochemical battery models, such as the Doyle-Fuller-Newman (DFN) model, are valuable tools for simulating Li-ion battery behavior and understanding internal battery processes. However, the complexity and computational demands of such models limit their applicability for battery management systems and long-term aging simulations. Reduced-order models (ROMs), such as the Extended Single Particle Model (ESPM), Single Particle Model (SPM) and Polynomial and Padé approximations, here all referred to as simplifications, lead to faster computational speeds. Choosing the appropriate simplification method for a specific cell type and operating condition is a challenge. This study investigates the simulation accuracy and calculation speed of various simplifications for high-energy (HE) and high-power (HP) batteries at different current loading conditions and compares those to the full-order DFN model. The results indicate that among the ROMs, the ESPM consistently offers the best combination of high computational speed and relatively good accuracy in most conditions in comparison to the full-order DFN model. Among the approximations, higher-order polynomial approximation, third and fourth-order Padé approximation perform the best in terms of accuracy. The higher-order polynomial approximation shows an advantage in terms of computing speed, while the fourth-order Padé approximation achieves the highest overall accuracy among the different approximations.

1. Introduction

Li-ion batteries (LIBs) play a crucial role in the electrification of transportation [1] and energy storage for smart grid applications [2]. Battery management systems (BMSs) are a key component for ensuring safe operation and maximizing LIB lifetime [3–6]. One of the core functions of a BMS is battery state estimation, wherein the BMS evaluates internal battery states, such as the state-of-charge (SoC), state-of-health (SoH) and state-of-power [7]. Battery state information is the basis for BMS control functions, such as temperature management, cell balancing and current limits during (dis)charge processes [8]. The control capability of a BMS therefore depends on the accuracy of its battery state estimation which, in turn, depends on the accuracy of the implemented BMS battery model. Various types of battery models are commonly applied to enhance the performance of BMSs, which essentially can be categorized into three common types: data-driven, semi-empirical and physics-based models.

Data-driven approaches, also known as black box models, employ machine learning techniques to estimate LIB states [9]. Prominent examples of such models include neural networks [10,11], gaussian regression [12–14] and support vector machines [15–17], which have recently gained popularity. The advantage of data-driven models is their ability to estimate complex battery dynamics with relatively low computational power, which makes them ideal for BMS applications. However, data-driven models struggle with generalization, lack physical insights and rely heavily on training data quality and representativeness, which can pose challenges when working with limited or biased datasets [18,19]. In recent studies, physics-based battery models have been used to generate training data for the data-driven models [20,21]. This

---

Abbreviation: BMS, Battery management system; CC, Constant current; DFN, Doyle-Fuller-Newman; ESPM, Extended Single Particle Model; EV, Electric vehicle; FDM, Finite difference method; FVM, Finite volume method; HE, High-energy; HP, High-power; HPA, Higher-order polynomial approximation; LIB, Li-ion battery; P2, Second-order Padé approximation; P2D, Pseudo-two-dimensional; P3, Third-order Padé approximation; P4, Fourth-order Padé approximation; RMSE, Root mean squared error; ROM, Reduced-order mode; SoC, State of charge; SoH, State of health; SPM, Single Particle Model; TPA, Two-parameter polynomial approximation; WLTP, Worldwide Harmonized Light Vehicles Test Procedure.

[*] Corresponding author.
E-mail address: l.raijmakers@fz-juelich.de (L.H.J. Raijmakers).

https://doi.org/10.1016/j.electacta.2024.144360
Received 23 February 2024; Received in revised form 16 April 2024; Accepted 27 April 2024

Nomenclature

a_{EV}	Acceleration, m s^{-2}
A_f	Frontal area, m^2
a_s	Specific interfacial surface area, m^{-1}
A_{surf}	Electrode surface area, m
b	Bruggeman exponent, -
C_d	Drag coefficient, -
c_e	Concentration in the electrolyte phase, mol m^{-3}
$c_{e,0}$	Initial electrolyte concentration, mol m^{-3}
C_r	Rolling friction coefficient, -
c_s	Concentration in the solid phase, mol m^{-3}
c_s^{avg}	Average concentration in the solid phase, mol m^{-3}
c_s^{max}	Maximum concentration in the solid phase, mol m^{-3}
c_s^{surf}	Surface concentration in the solid phase, mol m^{-3}
D_e	Diffusion coefficient in electrolyte phase, m^{2}s^{-1}
D_s	Diffusion coefficient in the solid phase, m^{2}s^{-1}
$E_{battery}$	Energy density, Wh kg^{-1}
F	Faraday constant, 96,487 C mol^{-1}
$f_\pm$	Mean molar activity coefficient of the electrolyte, -
g	Gravitational acceleration, 9.81 m s^{-2}
i_0	Exchange current density, A m^{-2}
I_{app}	Applied current, A
j_{Li}	Molar ionic flux, mol m^{-2}s^{-1}
k_0	Reaction rate coefficient, mol$^{-3/2}$m$^{-1/2}$s^{-1}
L	Overall thickness of the cell, m
m	Mass, kg
MSS	Magnitude of simulation speed,%
P_{EV}	Propulsion power, W
q^{avg}	Volume-average concentration flux, mol m^{-4}
R	Universal gas constant, 8.314 J mol^{-1}K^{-1}
r	Radial position across a spherical particle, m
R_{cc}	Contact resistance, Ω m^2
R_s	Radius of particle, m
s	Frequency domain, -
T	Temperature, K
t	Time, s
t_+^0	Transference number
t_f	Simulation time of the reference model, s
t_s	Simulation time of the simplified models, s
U	Equilibrium potential of the electrode, V
V_{cell}	Battery output voltage, V
v_{EV}	Velocity, m s^{-1}
x	Position across cell layers, m
Greek	
α_a	Anodic charge-transfer coefficients, -
α_c	Cathodic charge-transfer coefficients, -
δ	Thickness, m
ε_e	Electrolyte volume fraction, -
ε_s	Active material volume fraction, -
η	Electrode overpotential, V
η_{EV}	Drive train efficiency, -
κ_e	Ionic conductivity, S m^{-1}
ν	Thermodynamic factor, -
ρ_{air}	Density of air, 1.2 kg m^{-3}
σ_s	Solid phase electronic conductivity, S m^{-1}
θ_{EV}	Angle of the slope, rad
θ	State vector, mol m^{-2}s^{-1}
ϕ_e	Electrolyte phase potential, V
ϕ_e^{mean}	Mean electrolyte phase potential, V
ϕ_s	Solid phase potential, V

approach becomes more efficient, cost-effective, and time-saving, thus mitigating one of the disadvantages associated with data-driven models.

Semi-empirical models, often referred to as gray box models, use experimental data to derive empirical equations through fitting in order to predict LIB behavior [22]. The most prominent example is the equivalent circuit model (ECM) [23–25]. The advantages of the ECM are low computational power requirements and simplicity. However, the main disadvantage of ECMs is that they primarily estimate global values, such as output voltage, battery temperature, SoC and SoH and lack local ionic concentration and potential information through the battery cell layers. This results in insufficient physical information, which is critical for monitoring battery behavior and state estimation for advanced BMSs [26–28].

The physics-based battery models are models describing the kinetic, thermodynamic, transport and mechanical processes in batteries [29]. Because of the rigorous description of the underlying phenomena, physics-based battery models can predict LIB performance with high accuracy and provide insight into the internal physical and electrochemical processes [22,30,31]. In addition, LIB temperature evolution can be accurately described in temperature-dependent models, thereby aiding in preventing accelerated aging and mitigating thermal runaway [32–35].

As a result, physics-based models have shown outstanding agreement with experimental results [36–38]. The most popular physics-based model for LIBs is based on the pseudo-two-dimensional (P2D) model framework, which is also known as the Doyle-Fuller-Newman (DFN) model, on account of the pioneering developers of this model [39,40]. However, due to its complexity and high computational demand, the DFN model may not be feasible for BMS applications and long-term aging simulations.

Simulating the intercalation mechanism within the electrode active particles, as described by Fick's second law for diffusion, represents one of the most computationally intensive processes [41–43]. This has led to the development of various approximation models for simulating diffusion inside the solid particles with the aim of reducing the aforementioned computational burden. One of the approximation methods resolves the solid phase diffusion problem with a polynomial approach, leading to two-parameter polynomial approximation (TPA) [44,45] and higher-order polynomial approximation (HPA), also referred to as three-parameter polynomial approximation [41,42,46,47]. Another method is to use the Padé approximation, solving Fick's second law for solid particles with a rational function [43,48–50]. Further approximation techniques were applied through the Galerkin projection method, balanced truncation and proper orthogonal decomposition [43]. While similar approximation methods can be found in the literature [51–53] for solving electrolyte phase diffusion equations, the primary focus lies in addressing solid-state diffusion due to its significantly higher computational intensity.

A very popular approach for increasing computational speed is by simplifying the DFN model to the so-called single particle model (SPM) [49–51,54–59]. In the SPM approach, each electrode is considered as a single spherical porous particle in which electrolyte dynamics are neglected. However, this approach might lead to rather inaccurate simulation results, especially at higher C-rates. The accuracy of the SPM can be further improved by the incorporation of electrolyte dynamics. This results in an extended single particle model (ESPM), which generally has higher simulation accuracy than the SPM [43,45,47,48,51,52,54,57,60–62]. In this work, both the SPM and ESPM are classified as reduced-order models (ROMs) while the DFN model is classified as the full-order model.

On top of the physics-based modeling approaches (i.e., DFN, SPM, ESPM), a multitude of approximations are possible and, therefore, evaluating simulation accuracy and computational speed is essential for choosing the right simplification, where the simplification can be a ROM, an approximation, or a combination of both. A comparison of various physics-based ROMs and approximation techniques can be found in Table 1. From this table, it becomes apparent that there is a lack of comprehensive studies comparing the various approximation methods in combination with the various ROMs. Moreover, most studies only use one battery type or one set of parameters for model evaluation, which limits insights in how the various models perform with different battery types, such as high-energy (HE) or high-power (HP) batteries. Although review papers on model simplifications can be found in the literature [22,63–67], these do not adequately address the comparison of ROMs and model approximations due to variations in battery parameters and conditions among the cited work. In addition, Table 1 shows that models are often evaluated under current loading conditions, especially constant current (CC) discharge. Therefore, there are hardly any insights into ROM and model approximation performance in the relaxation region, which is often a region with lower simulation accuracy, especially at low and high SoC values [68].

Table 1
An overview of various physics-based battery model simplifications.

Model + ROMs	Solid phase Li-ion concentration approximation	Parameter sets	Evaluation method	Reference
DFN + ESPM	–	1	CC-discharge + dynamic cycle	[62]
DFN + ESPM	–	1	CC-discharge	[52]
DFN + ESPM	TPA	2	CC-discharge + dynamic cycle	[45]
DFN + ESPM + SPM	–	1	CC-discharge + dynamic cycle	[54]
DFN + ESPM + SPM	–	1	CC-discharge	[61]
ESPM	Padé approximation	1	Dynamic cycle	[48]
DFN + SPM	TPA + HPA	1	Dynamic cycle	[42]
ESPM + SPM	–	1	CC-discharge + drive cycle	[60]
SPM	Padé approximation	1	CC-discharge	[69]
DFN	TPA + HPA	1	CC-discharge	[41]
DFN + SPM	TPA + HPA	1	CC-discharge/ charge + dynamic cycle	[47]
ESPM	Padé approximation + Galerkin projection method + Balanced truncation + Proper orthogonal decomposition	1	Dynamic cycle	[43]
DFN + ESPM + SPM	–	1	CC-discharge/ charge + dynamic cycle	[51]
DFN + ESPM + SPM	–	1	CC-discharge	[57]
SPM	Padé approximation	1	CC + constant voltage	[50]
DFN + SPM	–	2	CC-discharge + dynamic cycle	[70]
DFN + ESPM + SPM	TPA + HPA + Padé approximation	2	CC-discharge + Relaxation + dynamic cycle	Present work

In this study, the simulation speed and accuracy of various approximations, ROMs and a combination of both are evaluated in comparison to the physics-based, full-order DFN model from Refs. [40,41]. By comparing these simplifications, a more comprehensive understanding of model performance in the discharge and relaxation phases, as well as during a dynamic cycle, can be obtained. It should be noted that three model approximation techniques are used in this study: TPA, HPA and Padé approximation. Fan et al. [43] (Table 1) compared various approximation techniques and concluded that Padé approximation was most favorable in terms of accuracy and speed in comparison to Galerkin, balanced truncation and orthogonal decomposition. For this reason, we selected Padé approximation, TPA and HPA. Furthermore, the parameter sets of both a HE and HP battery are considered to investigate model performance for different battery types. Node optimization in the electrodes, separator and solid particles has been applied to ensure an unbiased and fair comparison among the model simplifications. Additionally, a sensitivity analysis explores how model parameters affect DFN model and ROM sensitivity.

2. Theoretical considerations

This section outlines the theoretical underpinnings of the DFN model alongside its ROMs and approximations for solid-phase concentration. Furthermore, insights are offered into the model's implementation and comparison methodologies for assessing computational speed and accuracy.

2.1. Electrochemical modeling

A typical LIB is made up of two current collectors, a porous negative electrode (anode), and a porous positive electrode (cathode), as illustrated in the schematic overview of an LIB in Fig. 1. The active materials within the electrodes are represented as green and purple spherical particles, while additives and binders are denoted by small red and blue particles, respectively. The schematic representation of the DFN model, based on porous electrode theory, is shown in Fig. 1b. In this model, each electrode is considered as a collection of macro homogeneous spherical particles. The model describes the dynamics within the battery cell in two dimensions. The first dimension, represented as the x-dimension, includes the thickness of the various cell layers on the macroscopic level through which the mass transfer, electric potential in the solid and electrolyte are simulated. These layers include the negative electrode thickness (δ_n), the separator thickness (δ_s), the positive electrode thickness (δ_p) and the overall thickness of the cell (L) but is excluding the current collectors. The second dimension, referred to as the r-dimension, can be considered on the microscopic scale and represents the (average) particle radius of the negative electrode ($R_{s,n}$) and positive electrode ($R_{s,p}$). In essence, the DFN model represents battery behavior by considering both the macroscopic layer thickness and the microscopic particle radius of the electrodes. Assuming that each electrode can be represented by one spherical particle, instead of multiple particles, the DFN model reduces to an ESPM, shown in Fig. 1c. When further neglecting the electrolyte dynamics, the ESPM simplifies into the SPM, as illustrated in Fig. 1d.

2.1.1. DFN model

The DFN model is governed by four non-linear partial differential equations (PDEs) that capture the conservation of mass and charge in both the solid and electrolyte phases of LIBs. The concentration profile of Li-ions in the solid phase (c_s) of both electrodes is governed by Fick's second law of diffusion, represented by

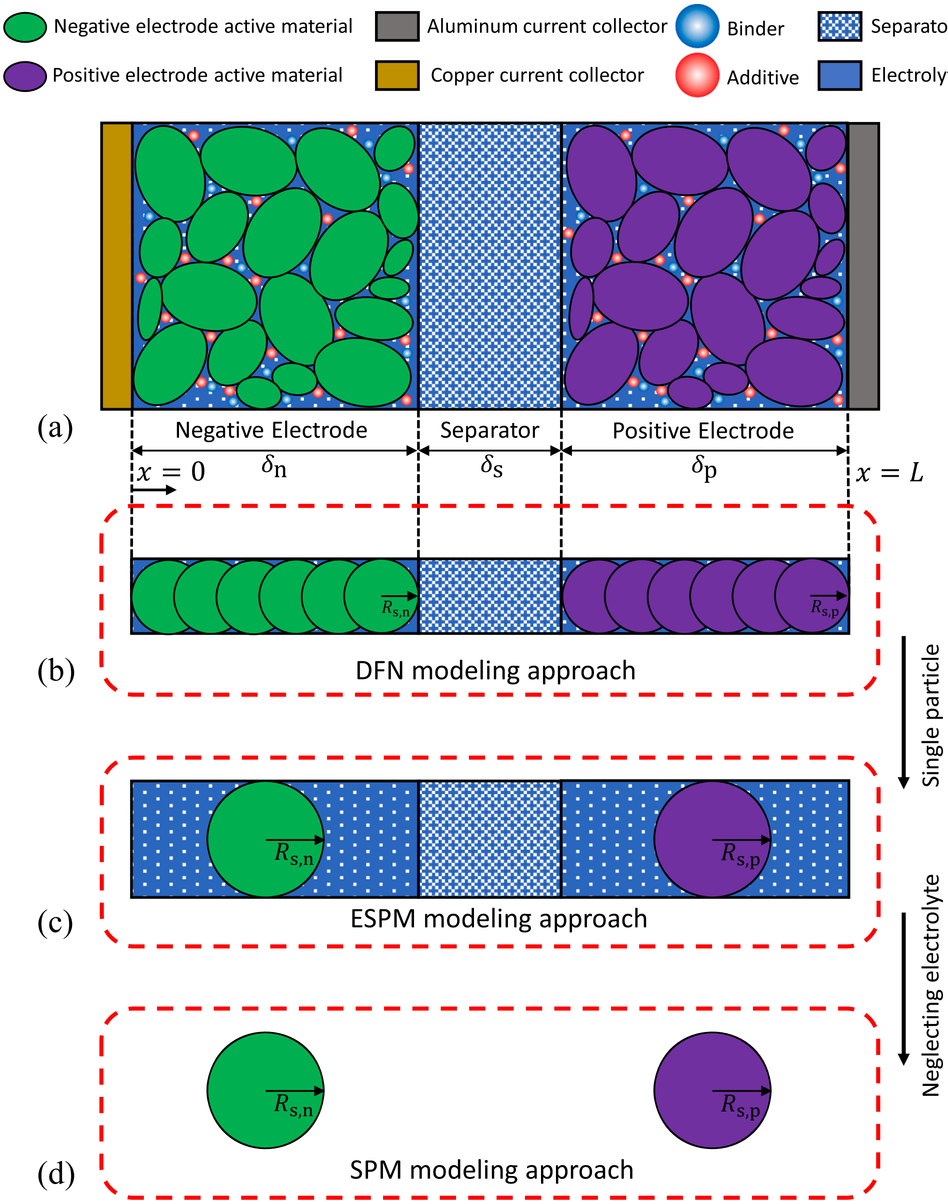

Fig. 1. Schematic illustration of a LIB (a) and the DFN (b), ESPM (c) and SPM (d) modeling approaches.

$$\frac{\partial c_s(r,t)}{\partial t} = \frac{D_s}{r^2}\frac{\partial}{\partial r}\left(r^2 \frac{\partial c_s(r,t)}{\partial r}\right), \quad r \in [0, R_s], \tag{1a}$$

with boundary conditions

$$\left.\frac{\partial c_s(r,t)}{\partial r}\right|_{r=0} = 0, \tag{1b}$$

$$-D_s \left.\frac{\partial c_s(r,t)}{\partial r}\right|_{r=R_s} = j_{Li}(x,t), \tag{1c}$$

where t is time, D_s the diffusion coefficient in the solid phase, R_s the particle radius and j_{Li} is the molar ionic flux. Eqs. (1b-1c) apply Neuman boundary conditions at the boundary ($r = R_s$) and center ($r = 0$) of the particle.

The Li-ion concentration in the electrolyte phase (c_e) of the porous electrode and separator regions can be calculated with

$$\varepsilon_e \frac{\partial c_e(x,t)}{\partial t} = \frac{\partial}{\partial x}\left(D_e \varepsilon_e^{b} \frac{\partial c_e(x,t)}{\partial x}\right) + a_s\left(1 - t_+^0\right) j_{Li}(x,t), \quad x \in [0, L], \tag{2a}$$

with boundary conditions

$$\left.\frac{\partial c_e(x,t)}{\partial x}\right|_{x=0} = \left.\frac{\partial c_e(x,t)}{\partial x}\right|_{x=L} = 0, \tag{2b}$$

where ε_e is the electrolyte volume fraction, b the Bruggeman exponent, D_e the diffusion coefficient of the electrolyte phase, a_s the specific interfacial surface area, which is calculated as $a_s = 3\varepsilon_s/R_s$, ε_s the active material volume fraction and t_+^0 is the transference number. These equations govern the transport of Li$^+$ ions within the electrolyte phase, capturing the movement of ionic species between the cathode and anode in both directions.

The solid phase potential (ϕ_s), which is the potential along the thickness of the two electrodes, is calculated by Ohm's law

$$\frac{\partial}{\partial x}\left(\sigma_s \varepsilon_s \frac{\partial \phi_s(x,t)}{\partial x}\right) = a_s F j_{Li}(x,t), \quad x \in [0, \delta_n] \cup \left[L - \delta_p, L\right], \tag{3a}$$

with boundary conditions

$$\sigma_s \varepsilon_s \frac{\partial \phi_s(x,t)}{\partial x}\bigg|_{x=0} = \sigma_s \varepsilon_s \frac{\partial \phi_s(x,t)}{\partial x}\bigg|_{x=L} = \frac{I_{app}(t)}{A_{surf}}, \tag{3b}$$

$$\frac{\partial \phi_s(x,t)}{\partial x}\bigg|_{x=\delta_n} = \frac{\partial \phi_s(x,t)}{\partial x}\bigg|_{x=L-\delta_p} = 0, \tag{3c}$$

where σ_s is the solid phase electronic conductivity, F the Faraday constant, I_{app} the applied current and A_{surf} is the electrode surface area.

The electrolyte phase potential (ϕ_e) is described by

$$\frac{\partial}{\partial x}\left(\kappa_e \varepsilon_e^b \frac{\partial \phi_e(x,t)}{\partial x} + \kappa_e \varepsilon_e^b \nu \frac{2RT(t)}{F} \frac{\partial \ln c_e(x,t)}{\partial x}\right) = -a_s F j_{Li}(x,t),\ x \in [0,L], \tag{4a}$$

with boundary conditions

$$\frac{\partial \phi_e(x,t)}{\partial x}\bigg|_{x=0} = \phi_e(x,t)|_{x=L} = 0, \tag{4b}$$

where κ_e is the electrolyte conductivity, R the universal gas constant and T is the absolute temperature. Additionally, ν is the thermodynamic factor calculated as $\nu = (1 - t_+^0)\left(1 + \frac{d\ln f_\pm}{d\ln c_e}\right)$, in which $f_\pm$ is the mean molar activity coefficient of the electrolyte [29].

The Butler-Volmer equation can be used for describing the electrochemical reaction-rate at the solid/electrolyte interface and relates the overpotential at the electrodes (η) with the j_{Li} for $x \in [0, \delta_n] \cup [L - \delta_p, L]$ as

$$j_{Li}(x,t) = \frac{i_0(x,t)}{F}\left(\exp\left(\alpha_a \frac{F}{RT(t)}\eta(x,t)\right) - \exp\left(\alpha_c \frac{F}{RT(t)}\eta(x,t)\right)\right) \tag{5a}$$

where the overpotential at the electrodes is

$$\eta(x,t) = \phi_s(x,t) - \phi_e(x,t) - U(x,t), \tag{5b}$$

the exchange current density is

$$i_0(x,t) = k_0(c_e(x,t))^{\alpha_a}\left(c_s^{max} - c_s^{surf}(x,t)\right)^{\alpha_a}\left(c_s^{surf}(x,t)\right)^{\alpha_c}, \tag{5c}$$

and the battery voltage is

$$V(t) = \phi_s(L,t) - \phi_s(0,t) - \frac{R_{cc}}{A_{surf}} I_{app}(t)\ . \tag{5d}$$

In Eq. (5), α_a and α_c are the anodic and cathodic charge-transfer coefficients, respectively, U is the equilibrium potential of the electrode, which is in modeling work often defined as a predefined nonlinear function of the stoichiometry. Furthermore, k_0 is the reaction-rate constant of the electrochemical reaction, c_s^{max} is the maximum ionic concentration in the solid phase and R_{cc} is the contact resistance. A flux of Li-ions leaving the solid particle occurs when $j_{Li} > 0$ and entering the solid particle when $j_{Li} < 0$. In the separator region, where no particles are present, $j_{Li} = 0$.

2.1.2. Reduced-order models

ROMs are used to simplify representations of high-dimensional systems, preserving essential behavior for maintaining accuracy while reducing computational complexity for improving simulation speed. The SPM and ESPM are classified as ROMs. The SPM is a ROM in which each electrode is considered as a single spherical particle and where electrolyte dynamics are neglected. The SPM is derived based on the following assumptions:

- c_s remains constant along the spatial coordinate x in both electrodes.
- i_0 is independent of the spatial coordinate x and only varies with time.
- The charge-transfer coefficients α_a and α_c are typically assumed to be 0.5.

As a result of the initial two assumptions, the interfacial flux of Li$^+$ ions at the solid/electrolyte interface remains constant across each electrode. Therefore, for the SPM, j_{Li} can be calculated for the negative and positive electrode with

$$j_{Li}(t) = -\frac{I_{app}(t)}{A_{surf} a_{s,n} \delta_n F}, \tag{6a}$$

and

$$j_{Li}(t) = \frac{I_{app}(t)}{A_{surf} a_{s,p} \delta_p F}, \tag{6b}$$

respectively. As a result of these assumptions, the simplified electrode overpotential is obtained with

$$\eta(t) = \sinh^{-1}\left(\frac{j_{Li}(t)F}{i_0(t)}\right) * \frac{RT(t)}{F}, \tag{7}$$

where i_0 is calculated from Eq. (5c) with the assumption of c_e being set as constant value using the initial electrolyte concentration ($c_{e,0}$). Of all PDEs in Section 2.1.1, only the PDE in Eq. (1) needs to be used for the SPM.

The SPM can be extended by implementing electrolyte dynamics, resulting in the ESPM, which combines a single particle model for both electrodes along with electrolyte dynamics and uses the PDEs as described in Eqs. (1), (2) and (4). In addition, the total concentration of Li$^+$ ions in the electrolyte and the solid are conserved and treated separately in each phase. Consequently, the electrode overpotential from Eq. (7) needs to be modified with the mean electrolyte phase potential (ϕ_e^{mean}), giving

$$\eta(t) = \sinh^{-1}\left(\frac{j_{Li}(t)F}{i_0(t)}\right) * \frac{RT(t)}{F} + \phi_e^{mean}(t)\ . \tag{8}$$

where j_{Li} can be obtained from Eqs. (6a-b).

Table 2 gives an overview of the PDEs used for the SPM, ESPM and DFN models. From this table, it can be seen that the DFN model makes use of all PDEs, while the SPM only makes use of one PDE, making the SPM computationally faster, but also less accurate. The SPM approach leads to 17 necessary model parameters. These parameters are listed in Table 3 and structured in various groups: geometric, transport, kinetic, concentration and thermodynamic. Note that in Table 3, not all the 17 SPM parameters are shown because various parameters occur twice, i.e., for both electrodes. Obviously, this also holds for the DFN and the ESPM. The ESPM, which has fewer simplifications than the SPM, but still being a simplified version with respect to the DFN model, requires a set of 27 parameters. The DFN model in this study uses a total of 31 parameters and thus has the most parameters of all three models. The difference in the number of parameters reflects the level of complexity and order reductions implemented in each model, which gives room for making trade-offs between accuracy and computational efficiency. However, these trade-offs are nontrivial and need to be carefully considered per application. This means, for example, a HP battery can be simulated with a different model in comparison to a HE battery, while obtaining the same level of accuracy.

Table 2
Overview of PDEs required for the SPM, ESPM and DFN models. The ✓ and × symbols indicate whether a particular governing equation is required or not.

Governing equation	Eq.	SPM	ESPM	DFN
Concentration of Li$^+$ ions in the solid phase	(1)	✓	✓	✓
Concentration of Li$^+$ ions in the electrolyte phase	(2)	×	✓	✓
Electrolyte phase potential	(4)	×	✓	✓
Solid phase potential	(3)	×	×	✓

Table 3
Overview of the parameters required for the SPM, ESPM and DFN models. The ✓ and × symbols indicate whether a particular parameter is required or not.

Group	Parameter	SPM	ESPM	DFN
Geometric	δ	✓	✓	✓
	A_{surf}	✓	✓	✓
	ε_{s}	✓	✓	✓
	ε_{e}	×	✓	✓
	R_{s}	✓	✓	✓
Transport	D_{s}	✓	✓	✓
	D_{e}	×	✓	✓
	σ_{s}	×	×	✓
	κ_{e}	×	✓	✓
	b	×	✓	✓
	t_{+}^{0}	×	✓	✓
Kinetic	k_0	✓	✓	✓
	R_{cc}	✓	✓	✓
	α	×	×	✓
Concentration	$c_{\mathrm{s}}^{\max}$	✓	✓	✓
	$c_{\mathrm{e},0}$	✓	✓	✓
Thermodynamics	U	✓	✓	✓

2.1.3. *Solid phase concentration approximations*

On top of all models, including the ROMs, approximations of the Li-ion solid phase concentration (Eq. (1)) can be made. Approximations simplify mathematical expressions or systems to obtain practical solutions without the need for complex computations. The approximations for the solid phase lithium concentration are based on the primary assumption that the diffusion dynamics within the solid particles result in the heaviest computational burden. By approximating the diffusion dynamics, a substantial increase in simulation speed can be achieved. As shown in Table 1, polynomial and Padé methods are commonly implemented for such approximations, which are also adopted in this study.

The concentration profile inside the particle can be approximated using polynomial approximation [46]. The TPA for the solid phase concentration is defined as

$$\frac{dc_{\mathrm{s}}^{\mathrm{avg}}(x,t)}{dt}=\frac{-3}{R_{\mathrm{s}}}j_{\mathrm{Li}}(x,t), \tag{9a}$$

and

$$c_{\mathrm{s}}^{\mathrm{surf}}(x,t)=c_{\mathrm{s}}^{\mathrm{avg}}(x,t)-\frac{R_{\mathrm{s}}}{5D_{\mathrm{s}}}j_{\mathrm{Li}}(x,t)\ . \tag{9b}$$

Eq. (9a) calculates the average concentration in the solid phase ($c_{\mathrm{s}}^{\mathrm{avg}}$), while Eq. (9b) calculates the surface concentration in the solid phase ($c_{\mathrm{s}}^{\mathrm{surf}}$). Alternatively, the HPA can be used, which is defined as

$$\frac{\partial c_{\mathrm{s}}^{\mathrm{avg}}(x,t)}{\partial t}=\frac{-3}{R_{\mathrm{s}}}j_{\mathrm{Li}}(x,t), \tag{10a}$$

$$\frac{\partial q^{\mathrm{avg}}(x,t)}{\partial t}=-30\frac{D_{\mathrm{s}}}{R_{\mathrm{s}}^{2}}q^{\mathrm{avg}}(x,t)-\frac{45}{2}\frac{j_{\mathrm{Li}}(x,t)}{R_{\mathrm{s}}^{2}}, \tag{10b}$$

$$c_{\mathrm{s}}^{\mathrm{surf}}(x,t)=c_{\mathrm{s}}^{\mathrm{avg}}(x,t)-\frac{R_{\mathrm{s}}}{35D_{\mathrm{s}}}j_{\mathrm{Li}}(x,t)+8R_{\mathrm{s}}q^{\mathrm{avg}}(x,t), \tag{10c}$$

where q^{avg} is the volume-average concentration flux.

Another approach for simplifying the solid phase concentration involves the utilization of Padé approximation [34]. Padé approximation is a technique that approximates a function using a rational polynomial centered around a specific point. A transfer function in the frequency domain (s), representing the solid phase concentration, can be obtained by applying a Laplace transformation to Eq. (1). To simplify this transfer function, Padé approximation can be used to derive an approximation of arbitrary order that covers a specific frequency range, determined by the order of the transfer function. In diffusion-based problems, the focus is often on low-frequency behavior, leading to an approximation approaching zero [43,50,71]. The transfer functions for $c_{\mathrm{s}}^{\mathrm{avg}}$ and $c_{\mathrm{s}}^{\mathrm{surf}}$ are defined by

$$\frac{c_{\mathrm{s}}^{\mathrm{avg}}(x,s)}{j_{\mathrm{Li}}(x,s)}=\frac{\int_0^{R_{\mathrm{s}}}c_{\mathrm{s}}(r,t)(4\pi r^2dr)}{(4/3)\pi R_{\mathrm{s}}^3}=-\frac{3}{a_{\mathrm{s}}FR_{\mathrm{s}}s}, \tag{11a}$$

and

$$\frac{c_{\mathrm{s}}^{\mathrm{surf}}(x,s)}{j_{\mathrm{Li}}(x,s)}=\frac{a_0+a_1s+a_2s^2+\ldots+a_{n-1}s^{n-1}}{s(1+b_2s+b_3s^2+\ldots+b_{\mathrm{n}}s^{n-1})}, \tag{11b}$$

respectively, where the coefficients a_{n} and b_{n} are dependent on the order of the Padé approximation. In this study the second-order (P2), third-order (P3) and fourth-order (P4) are selected to enable a comprehensive comparison across a wide range, for which the elaborated versions can be found in Table 4.

For an easy implementation of the Padé approximation, the transfer function can be transformed into a state-space representation, which is defined by

$$\frac{\partial\theta(x,t)}{\partial t}=\begin{bmatrix}0&1&0&0&\cdots&0\\0&0&1&0&0&0\\0&0&0&\ddots&0&0\\\vdots&\vdots&\vdots&\vdots&1&0\\0&0&0&0&0&1\\0&-\frac{1}{b_{\mathrm{n}}}&-\frac{b_2}{b_{\mathrm{n}}}&-\frac{b_3}{b_{\mathrm{n}}}&\cdots&-\frac{b_{n-1}}{b_{\mathrm{n}}}\end{bmatrix}\theta(x,t)+\begin{bmatrix}0\\0\\0\\\vdots\\0\\1\end{bmatrix}j_{\mathrm{Li}}(x,t), \tag{12a}$$

$$\begin{bmatrix}c_{\mathrm{s}}^{\mathrm{avg}}(x,t)\\c_{\mathrm{s}}^{\mathrm{surf}}(x,t)\end{bmatrix}=\begin{bmatrix}\frac{a_0b_1}{b_{\mathrm{n}}}&\frac{a_0b_2}{b_{\mathrm{n}}}&\cdots&\frac{a_0b_{\mathrm{n}}}{b_{\mathrm{n}}}\\\frac{a_0}{b_{\mathrm{n}}}&\frac{a_1}{b_{\mathrm{n}}}&\cdots&\frac{a_{n-1}}{b_{\mathrm{n}}}\end{bmatrix}\theta(x,t), \tag{12b}$$

$$\theta_{\mathrm{init}}(x,t)=\begin{bmatrix}c_{\mathrm{s,init}}^{\mathrm{surf}}(x,t)\frac{b_{\mathrm{n}}}{a_0}&0&\cdots&0\end{bmatrix}^T, \tag{12c}$$

where θ is the state vector, for which the initial values (Eq. (12c)) are determined based on the initial concentration in the solid phase [72]. The conversion from a transfer function to a state-space model is widely used in control system analysis and design. The derived state-space set calculates the concentrations $c_{\mathrm{s}}^{\mathrm{surf}}$and $c_{\mathrm{s}}^{\mathrm{avg}}$ from Eq. (12b). Note that for the DFN approach $j_{\mathrm{Li}}(x,t)$ in Eq. (12a) is calculated from Eq. (5a), while for the SPM or ESPM approaches it's calculated as $j_{\mathrm{Li}}(t)$, using Eqs. (6a-b).

2.2. *Model implementation*

A combination of spatial and temporal discretization methods is employed to solve the PDEs given in Eqs. (1) to (4). The finite difference

Table 4
Padé approximations of $c_{\mathrm{s}}^{\mathrm{surf}}$ in Eq. (11b) for three orders.

Order	Transfer function
Second (P2)	$\dfrac{\frac{3}{R_{\mathrm{s}}}+\frac{2R_{\mathrm{s}}}{7D_{\mathrm{s}}}s}{s\left(1+\frac{R_{\mathrm{s}}^2}{35D_{\mathrm{s}}}s\right)}$
Third (P3)	$\dfrac{\frac{3}{R_{\mathrm{s}}}+\frac{4R_{\mathrm{s}}}{11D_{\mathrm{s}}}s+\frac{R_{\mathrm{s}}^3}{165D_{\mathrm{s}}^2}s^2}{s\left(1+\frac{3R_{\mathrm{s}}^2}{55D_{\mathrm{s}}}s+\frac{R_{\mathrm{s}}^4}{3465D_{\mathrm{s}}^2}s^2\right)}$
Fourth (P4)	$\dfrac{\frac{3}{R_{\mathrm{s}}}+\frac{2R_{\mathrm{s}}}{5D_{\mathrm{s}}}s+\frac{2R_{\mathrm{s}}^3}{195D_{\mathrm{s}}^2}s^2,+\frac{4,R_{,\mathrm{s}}^{5,}}{7,507,5D_{,\mathrm{s}}^{,3}}s^3}{s\left(1+\frac{R_{\mathrm{s}}^2}{15D_{\mathrm{s}}}s+\frac{2R_{\mathrm{s}}^4}{2275D_{\mathrm{s}}^2}s^2,+\frac{,R_{\mathrm{s},}^{6},}{67,567,5D_{,\mathrm{s}}^{,3}}s^3\right)}$

method (FDM) [45,73] is used for the full-order DFN model to discretize Eq. (1) along the *r*-direction. For Eqs. (2) to (4) the finite volume method (FVM) is applied, using the harmonic mean to determine the boundary values between two neighboring control volumes [41]. The number of discretized points or nodes for the FDM and FVM grids is further explained in Section 3.3. The resulting system of differential-algebraic equations is solved using Newton's method of which the tolerance was set to 1×10^{-3} in all simulations. A more detailed description of Newton's method implemented for the DFN model can be found in Refs. [45, 73]. The simulation time-step is chosen to be 1 s and the model temperature is set to isothermal conditions of 25 °C. It should be noted, however, that isothermal conditions are not fully representing real-world behavior. Temperature variations can significantly influence battery performance, affecting parameters such as the reaction-rate coefficient, ionic conductivity, and diffusion coefficients in the solid- and electrolyte-phase. Model programming and simulations are performed using MATLAB R2021b. A computer with AMD Ryzen 7 5700 U CPU @ 1.8 GHz, 24 GB RAM and Windows operating system has been used. The full-order DFN model will be used as reference model for comparison with all simplifications in this study.

2.3. *Computational speed and model accuracy*

To evaluate the computational speed of the various simplified models, the magnitude of simulation speed (MSS) is used, which is defined as

$$\mathrm{MSS} = \left(\frac{t_\mathrm{f} - t_\mathrm{s}}{t_\mathrm{f}}\right) \times 100, \tag{13}$$

where t_f is the simulation time of the reference model and t_s the simulation time of the simplified models (ROMs and approximations). All reported simulation times have been obtained by averaging the duration of 10 simulation repetitions, with the simulation time measured without pre-memory allocation of variables.

To evaluate the model accuracy, the root mean squared error (RMSE) has been used, which is defined as

$$\mathrm{RMSE} = \sqrt{\sum_{m=1}^{N} \frac{(y_\mathrm{f} - y_\mathrm{s})^2}{N}}. \tag{14}$$

where y_f are the reference model output values, y_s the output values of the simplified model and N the number of simulated values.

3. Case studies

This section introduces the battery types utilized, emphasizing key parameter distinctions. Additionally, it delves into simulation studies, encompassing CC-simulations, dynamic simulations, node optimizations, sensitivity analysis methods, and parameter ranges.

3.1. *Battery types*

In this study, the parameter sets of a HE and HP battery are used, adopted from Refs. [68] and [74], respectively. The HE battery is a commercial cell from LG (LGM50), having a rated capacity of 5 Ah with NMC811 as the positive electrode material and a mixed graphite/silicon negative material [68]. The HP battery is as well a commercial cell (unspecified manufacturer), has a rated capacity of 28 Ah with NMC111 as cathode material and graphite as anode material. A comparison between the measured and simulated voltage for the two cells is presented in Fig. S1. The average RMSEs for the HE and HP batteries are 37 and 19 mV, respectively. The higher error observed in the HE battery compared to the HP battery can be attributed to several factors. In the HE battery, parameters such as particle radii and electrode thicknesses are typically larger, resulting in more pronounced concentration profiles within the solid-phase. This leads to higher overpotentials in the HE battery compared to the HP battery. Due to the larger and more complex concentration profiles, capturing these effects accurately in the model becomes more challenging. Consequently, higher RMSEs are expected in the HE battery simulations compared to the HP battery simulations. In both this work and the work of Ref [68], the HE model considers a negative electrode containing graphite active particles only, thus neglecting silicon and the hysteresis effect, which could lead to additional simulation inaccuracies for the HE battery. Furthermore, it should be noted that $D_{\mathrm{s,p}}$, $D_{\mathrm{s,n}}$, $k_{0,\mathrm{n}}$ and $k_{0,\mathrm{p}}$ are considered concentration independent and, therefore, set as constant values.

Table 5 shows the most distinct parameters for the HE and HP batteries. The most significant difference lies in the transport parameters and kinetics of the active electrode material for the HP battery. Additionally, the HP battery has a thinner electrode design to enhance power performance. However, it should be noted that the HP battery has a significantly lower energy density (E_{battery}) compared to the HE battery. Fig. 2 shows the full-order DFN model results for both battery types at various C-rates using the parameter values in Refs. [68] and [74]. The simulation results demonstrate that the overpotentials for the HE battery are far larger than those for the HP battery, which proves completely different battery behavior between both battery types.

3.2. *Simulation studies*

3.2.1. *CC-discharge and relaxation*

CC-discharge simulations at three C-rates, followed by relaxation periods, are performed to compare the simplified models with the DFN reference model under static conditions. For the HE battery, simulations are performed at 0.25, 0.5 and 1C, while for the HP battery, simulations are performed at 1, 2, and 3C. Before each discharge simulation, the initial SoC is set to 1, corresponding to a voltage of 4.18 V for the HE battery and 4.15 V for the HP battery. The cut-off voltages are set to 2.5 V and 3 V for HE and HP batteries, respectively. The CC-discharge is followed by a relaxation period during which no current is applied until the output voltage stabilized at a steady-state level.

3.2.2. *Dynamic cycle*

A current profile, obtained from a drive cycle, is used to compare the performance of the simplified models under dynamic current loading conditions. The Worldwide Harmonized Light Vehicles Test Procedure (WLTP) class 3b cycle is chosen, of which the speed profile is shown in Fig. 3a. The WLTP covers a comprehensive range of speeds, accelerations, decelerations and stops, resembling real-world driving conditions [75] and is therefore ideal for investigating dynamic model performance. The WLTP consists of four driving regions representing different scenarios: low speed (A1), medium speed (A2), high speed (A3) and

Table 5
Summary of the highest difference between the selected batteries. The *n* and *p* in subscript represent the negative and positive electrodes, respectively.

Parameter	HE [68]	HP [74]	Difference* [%]
$\sigma_{\mathrm{s,p}}$	0.18	10	5456
$k_{0,\mathrm{n}}$ (10^{-11})	0.835	1000	1769
$D_{\mathrm{s,p}}$ (10^{-14})	0.4	2.04	411
$\sigma_{\mathrm{s,n}}$	215	1000	365
$k_{0,\mathrm{p}}$ (10^{-11})	4.605	7.423	61
$R_{\mathrm{s,p}}$ (10^{-6})	5.22	2.13	59
δ_{s} (10^{-6})	12.0	18.7	56
E_{battery}**	267	134	50
δ_{n} (10^{-6})	85.2	46.6	45
δ_{p} (10^{-6})	75.6	43.0	43

* $\text{Difference} = \frac{|\mathrm{HE}_{\mathrm{Parameter}} - \mathrm{HP}_{\mathrm{Parameter}}|}{\mathrm{HE}_{\mathrm{Parameter}}} \times 100$

** $E_{\mathrm{battery}} = \frac{\text{Rated capacity} \times \text{Nominal battery voltage}}{\text{Battery weight}}$

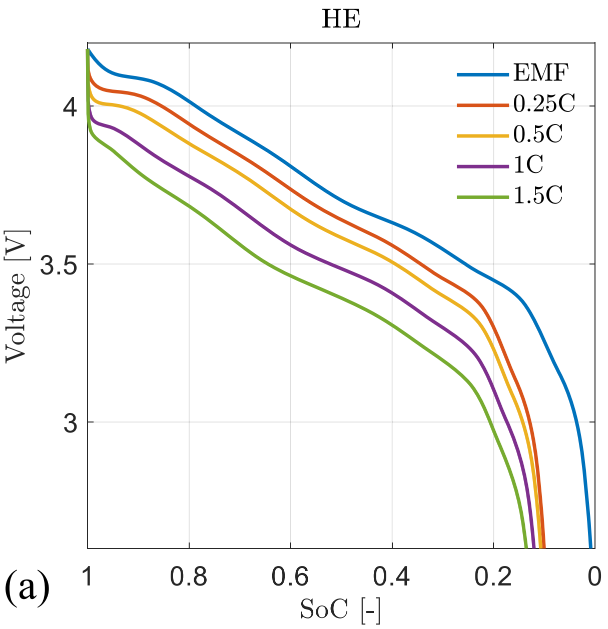

Fig. 2. Simulation results of discharge voltage curves for the HE (a) and HP (b) batteries at various C-rates, including electromotive force (EMF).

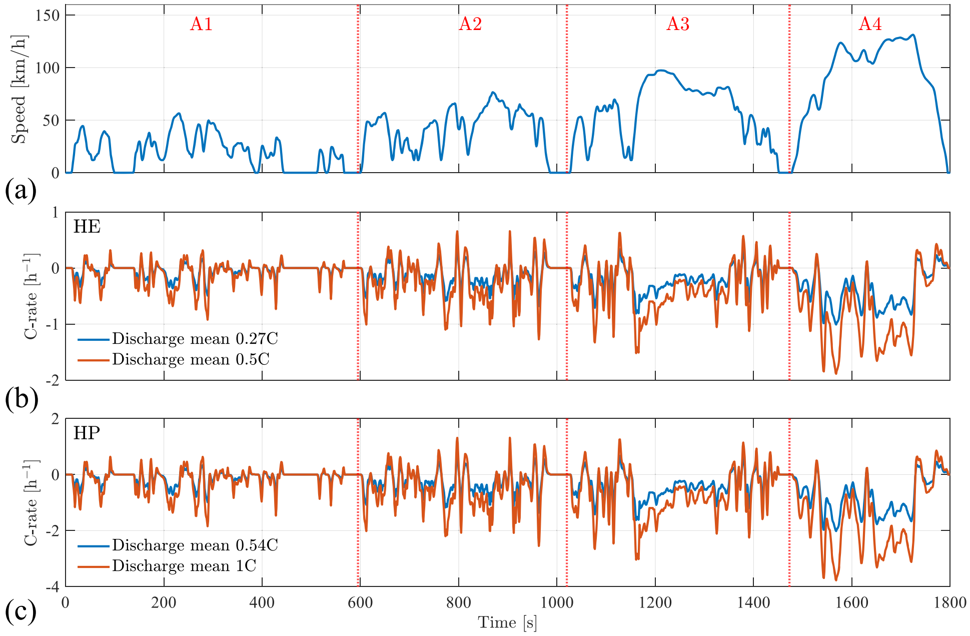

Fig. 3. WLTP cycle class 3b, speed (a), calculated C-rate for the HE battery (b) and HP battery (c) as a function of time.

extra high speed (A4).

The required propulsion power of an electric vehicle (EV) during the WLTP drive cycle can be calculated based on the forces, including the vehicle's rolling force, drag force and acceleration force. The required propulsion power (P_{EV}) can be estimated by

$$P_{\mathrm{EV}} = \left(C_{\mathrm{r}} mg\cos(\theta_{\mathrm{EV}}) + 0.5 C_{\mathrm{d}} A_{\mathrm{f}} \rho_{\mathrm{air}} v_{\mathrm{EV}}^2 + m a_{\mathrm{EV}}\right) * \frac{v_{\mathrm{EV}}}{\eta_{\mathrm{EV}}}, \tag{15}$$

where, C_{r} is the rolling friction coefficient, m the mass, g the gravitational acceleration, θ_{EV} the angle of the slope the vehicle is driving on, considered to be 0 in this study, C_{d} the drag coefficient, A_{f} the frontal area, ρ_{air} the density of air, v_{EV} the velocity, a_{EV} the acceleration and η_{EV} is the drive train efficiency. To calculate the propulsion power, the technical specifications from a Nissan Leaf e^+ have been used, which are shown in Table 6. Based on the calculated propulsion power and the battery specifications, the C-rate has been calculated, which is shown in Fig. 3b. The mean discharge C-rate for the HE battery is found to be 0.27C. Note that the mean C-rate has been calculated from discharge C-rates only. To evaluate the models at a higher C-rate, the standard C-rate additionally has been scaled to a mean discharge C-rate of 0.5C.

For model comparison of the HP battery type, the same profile should be applied. However, the C-rates of 0.27 and 0.5 are somewhat too mild for the HP battery and therefore the C-rates shown in Fig. 3b are scaled by a factor of two. This factor is determined from the difference in energy density between the HE and HP battery (see Table 5). Consequently, the C-rate for the WLTP cycle was adjusted to a mean discharge C-rate of 0.54 and 1, as shown in Fig. 3c. In all the simulations with the WLTP cycle, the initial SoC has been set to 0.5.

Table 6
Technical specifications for a Nissan Leaf e^{+} used for calculating the propulsion power and the C-rates in Fig. 3.

Parameter	Unit	Value	Reference
Vehicle mass	kg	1756	[76]
Frontal area	m^2	2.276	[77]
Drag coefficient	–	0.29	[78]
Rolling friction coefficient	–	0.012	[79]
Drive train efficiency	–	0.739	[79]
Battery pack energy	kWh	62	[76]
Battery pack nominal voltage	V	350	[76]
Number of cells in the pack	–	288	[76]
Cells in series	–	96	[76]
Cells in parallel	–	3	[76]
Cell Capacity	Ah	59	Estimated*

$^{*}\ \frac{\text{Battery pack energy}}{\text{Cells in parellel} \times \text{Battery pack nominal voltage}}.$

3.3. Node optimization

To ensure a fair comparison between the used models and to achieve high simulation accuracy with the highest simulation speed, the number of discretized points for the PDEs along the r and x-directions has been optimized, a process which is further referred to as node optimization. This optimization process determines the appropriate number of nodes, i.e., obtaining the fastest simulation time with an accuracy within a boundary. The nodes are equally distributed across five grids: the positive and negative electrode particles (r-direction), the positive and negative electrode, and the electrolyte (x-direction). Choosing a sufficiently large number of nodes leads to good accuracy while selecting a too large number of nodes results in increased computation time without a significant increase in accuracy. The optimization process has been performed by simulating the reference model with various numbers of nodes. To obtain accurate data for comparison, the reference DFN model has been simulated using a relatively high number of 50 nodes for both the FDM and FVM grids. Then, additional simulations have been performed with a number of nodes ranging between 6 and 50. The RMSE of the simulated output voltage has been compared to the reference voltage with a selected tolerance of 35 μV. The smallest number of nodes, with the simulated output voltage within the tolerance, has been selected. The optimized number of nodes have been applied to all models, including the simplified models.

Node optimization has been performed for both the HE and HP battery and for various operating conditions. Table 7 shows the optimized results. It can be seen that in the case of simulating a HE battery, the positive electrode and positive particle have a higher number of nodes compared to the negative side. This is primarily because the diffusion coefficient of the negative electrode is almost one order of magnitude larger than that of the positive electrode. Conversely, for the HP battery, the highest number of nodes is found in the negative particle. This is due to the relatively large particle radius compared to the positive counterpart, resulting in longer diffusion distances. Furthermore, it is worth noting that for both batteries and all operation conditions, the number of nodes in the separator region remains unchanged, with the optimal value determined to be the lowest of all regions. The reason is that the separator region is relatively thin, in which the electrolyte dynamics show almost linear behavior.

3.4. Sensitivity analysis

Sensitivity analysis plays a crucial role in identifying influential parameters that significantly impact the model output. Understanding the relative influence of the various model parameters makes optimizing or accurately estimating critical parameters easier. The sensitivity analysis in this study provides valuable insights into how model parameter changes affect the overall model behavior. A sensitivity analysis was conducted on the DFN, ESPM, and SPM models to compare their sensitivity to parameter changes and to evaluate the impact of simplifying the models by neglecting certain features. The QR factorization method [80] was employed, which assesses parameter correlations by measuring the extent to which the columns of the sensitivity matrix tend toward orthogonality through QR factorization. This process results in a parameter ranking, where dependent parameters receive lower rank and parameters demonstrating independence receive higher rank [81]. To assess the sensitivity of each parameter, a range of values is defined based on literature estimates for LIB parameters, which are shown in Table 8. A total of 25 parameters are used, where A_{surf}, α, $c_{\text{e},0}$ and U are excluded here. The sensitivity matrix of each model was orthogonalized with respect to the output voltage of the model to obtain the sensitivity of parameters. Further details about this method applied to battery models can be found in Refs. [82,83]. The sensitivity analysis is performed using a full 1 C-rate CC-discharge followed by a relaxation period of 15 min.

4. Simulation results

The DFN model is validated against a well-known, accurate DFN model from the LIONSIMBA toolbox [41]. Furthermore, the various ROMs and solid phase concentration approximations are evaluated based on the different conditions presented in Section 3. Additionally, the sensitivity analysis results are presented.

4.1. DFN model validation

Before starting to compare the models, the full-order DFN model (presented in Section 2) is validated using the LIONSIMBA toolbox and is further used as a reference model in this study [41]. The LIONSIMBA toolbox, which makes use of numerical calculation methods, contains the DFN model for LIBs in MATLAB, previously validated against a DFN model in COMSOL Multiphysics® [93]. The parameters used in the validation process are the same as those used in the LIONSIMBA model

Table 7
Optimized number of nodes for various operating conditions and battery types, which are used for all model types, including simplified models.

Battery type and operation condition	C-rate	Negative electrode	Positive electrode	Separator	Negative particle	Positive particle
HE (CC-discharge + relaxation)	0.25	10	34	6	20	28
	0.5	13	40	6	28	36
	1	18	44	6	33	42
HP (CC-discharge + relaxation)	1	8	9	6	45	6
	2	11	12	6	46	9
	3	13	15	6	47	12
HE (drive cycle)	0.27*	13	41	6	6	47
	0.5*	17	45	6	19	49
HP (drive cycle)	0.54*	8	10	6	22	11
	1*	11	13	6	31	14

* Mean discharge C-rate.

Table 8
Summary of parameter ranges for common type LIBs from literature.

Parameter	Values from literature	Range
δ_n (10^{-6})	46.6 [74], 50 [43,55], 62 [84], 67 [85], 73.7 [86], 81 [87], 85.2 [68], 88 [41], 96 [88]	46 – 96
δ_s (10^{-6})	12.0 [68], 18.7 [74], 19 [86], 20 [87], 24.4 [55], 25 [41,43,84,85,88]	12 – 25
δ_p (10^{-6})	36.4 [43,55], 43.0 [74], 54.5 [86], 60 [88], 74 [84], 75.6 [68], 78 [87], 79 [85], 80 [41]	36 – 80
$\varepsilon_{s,n}$	0.404 [86], 0.419 [85], 0.45 [84], 0.48 [43], 0.493 [74], 0.536 [88], 0.58 [55], 0.75 [68]	0.40 – 0.75
$\varepsilon_{s,p}$	0.375 [85], 0.38 [84], 0.3917 [86], 0.5 [43,55], 0.534 [88], 0.572 [74], 0.59 [41], 0.665 [68]	0.37 – 0.67
$\varepsilon_{e,n}$	0.25 [68], 0.264 [87], 0.292 [74], 0.329 [86], 0.332 [43,55], 0.4 [88], 0.485 [41], 0.5 [84]	0.25 – 0.50
$\varepsilon_{e,s}$	0.305 [74], 0.4 [88], 0.46 [87], 0.47 [68], 0.5 [43,55,84], 0.508 [86], 0.724 [41]	0.30 – 0.73
$\varepsilon_{e,p}$	0.209 [74], 0.281 [87], 0.296 [86], 0.33 [43,55], 0.335 [68], 0.36 [88], 0.385 [41], 0.45 [84]	0.20 – 0.45
$R_{s,n}$ (10^{-6})	1 [55], 2 [41], 3.5 [43], 5.86 [68], 6.3 [74], 8 [88], 8.7 [86], 10 [87], 11 [85]	1 – 11
$R_{s,p}$ (10^{-6})	1 [55], 2 [41,43], 2.13 [74], 5 [87,88], 5.22 [68], 6.49 [86], 7 [85]	1 – 7
$D_{s,n}$ (10^{-14})	1.5 [43], 1.75 [87], 3 [84], 3.21* [74], 3.3 [68], 3.9 [41], 7 [88], 8.8 [89]	1 – 9
$D_{s,p}$ (10^{-14})	0.4 [68], 1 [41], 1.35 [43], 2.04* [74], 3 [84,87,88], 8 [89]	0.4 – 8
D_e (10^{-10})	1.36* [90], 1.65* [91], 1.77* [68], 2.4 [86], 2.6 [55], 2.8* [88], 3.2* [92], 7.5 [41]	1.3 – 7.5
$\sigma_{s,n}$	14 [86], 100 [41,55,85,88], 215 [68], 1000 [74]	14 – 1000
$\sigma_{s,p}$	0.18 [68], 0.5 [88], 10 [55,74,85], 68.1 [86], 100 [41]	0.18 – 100
κ_e	0.205* [41], 0.787* [90], 0.932* [86], 0.949* [68], 0.95* [91], 1.105* [88], 1.17* [92]	0.2 – 1.11
b_n	1.5 [55,68], 1.52 [74]	1.3 – 1.7
b_s	1.44 [74], 1.5 [55,68,89]	1.3 – 1.7
b_p	1.5 [55,68], 1.62 [74]	1.3 – 1.7
t_+^0	0.2594 [68], 0.26 [74,86], 0.363 [55], 0.38 [84,89], 0.381*[92], 0.39 [43], 0.40*[88]	0.25 - 0.40
$k_{0,n}$ (10^{-11})	0.835 [68], 1.45 [86], 1.56 [74], 2 [84,85], 5.031 [41]	0.8 – 5.1
$k_{0,p}$ (10^{-11})	2 [84,85], 2.334 [41], 3.01 [86], 4.605 [68], 7.423 [74]	2 – 7.5
R_{cc} (10^{-3})	0.534 [74], 0.6 [87], 2 [55]	0.1 - 10
$c_{s,n}^{max}$ (10^3)	29.862 [85], 30.555 [41,89], 31.37 [84], 31.39 [74], 31.92 [86], 33.133 [68]	29 – 33.2
$c_{s,p}^{max}$ (10^3)	48.39 [74], 48.58 [86], 49.242 [85], 49.5 [89], 51.5 [84], 51.554 [41], 63.104 [68]	48 – 63.2

* Typical value at room temperature.

presented in Ref. [41]. To achieve accurate validation, an equal number of nodes has been set for both the DFN model in this study and the LIONSIMBA toolbox. In Fig. 4, simulation results of both models are shown for CC-discharge rates of 1, 2 and 3C. This comparison reveals that the two models show visually identical results for all states, such as voltages and concentrations. The RMSE values of the battery voltage in Fig. 4a are 0.06, 0.33 and 0.69 mV at 1, 2 and 3C-rate, respectively. Additionally, a comparison is performed with a pulsed cycle, revealing an RMSE of 0.42 mV. The simulation results of the pulsed cycle are shown in Fig. S2. The validation with LIONSIMBA assures that the implemented DFN model in this study is consistent with established models and that it can be used as a proper reference model.

4.2. *Evaluation of ROMs and approximations*

4.2.1. *CC-discharge and relaxation results*

Fig. 5 shows the simulation results of ROMs and approximations, in comparison to the reference DFN-model. Note that the most important selection of simplifications is shown and that the various approximations on the ROMs have been left out to not impede the figure. The results are shown for both the HE (Fig. 5a-c) and HP (Fig. 5d-f) batteries under various discharge C-rates. From a visual observation of the results can be concluded that the general CC-discharge and relaxation behavior are in line with the reference model, thereby validating the fidelity of the simplifications. However, looking into somewhat more detail, it becomes apparent that the SPM has the lowest agreement among the two ROMs. When comparing the SPM with the ESPM, it becomes evident that the accuracy significantly improves by adding the electrolyte dynamics. Both the SPM and ESPM demonstrate relatively large differences in the discharge region compared to the reference model, while showing good agreement in the relaxation region. The DFN model with the TPA and HPA methods shows relatively good agreement with the reference model at all C-rates for both the HE and HP battery. However, in the initial discharge and relaxation regions the DFN model with TPA has less agreement with the reference model compared to the DFN with HPA. The DFN model with Padé approximations (P2, P3 and P4) shows good agreement with the reference model, where the higher order Padé approximations obviously result in superior accuracy. This also holds true for the initial discharge and the relaxation regions. Supplementary Fig. S3 shows the error as a function of time.

From the results presented in Fig. 5, it can be concluded that the DFN model with P4 approximation is the most accurate model to be adopted, given its good accuracy. However, this is a provisional conclusion because no quantitative error and calculation speed is revealed yet. Therefore, for a more detailed and quantitative analysis of the differences between the reference model and simplifications, the RMSE has been calculated. Fig. 6 shows the total RMSE, which is the RMSE calculated for both the discharge and relaxation (blue bars), as well as the RMSE separately calculated for the discharge (orange bars) and relaxation regions (yellow bars). From the results in Fig. 6, it can immediately be seen that the RMSE increases with the C-rate (as indicated by the varying intensity in color shades) for all simplifications and batteries. This outcome can be attributed to the fact that the simplifications fail to capture the increased nonlinear dynamic behavior associated with higher C-rates. In general, the RMSE in the discharge region is lower for the HP battery compared to the HE battery, even though the HP battery is simulated at higher C-rates. The lower RMSE can be attributed to the specific HP battery parameters (Table 5), such as the relatively high solid phase electronic conductivity and thin electrode thickness, being advantageous for the ROMs. These properties lead to a relatively uniform potential distribution across the electrode thickness, which is also shown in supplementary Fig. S4. From the RMSE results, it can be clearly seen that the SPM and ESPM show the largest errors in the discharge region for both battery types, as also already concluded from Fig. 5. Another general trend, visible from Fig. 6, is that the RMSE decreases as a function of model order.

When considering the approximations, then TPA has the least overall accuracy for both batteries, although the accuracy for the discharge region for a HP battery is fairly accurate. The RMSEs for the HPA and P2 approaches are quite similar. Therefore, regarding accuracy, it is of less relevance if a HPA or P2 approximation approach is adopted. The DFN model with Padé approximations shows remarkable accuracy in the discharge region for the HP battery. However, in the relaxation region for the HP battery, the Padé approximations show relatively high RMSE values, for P2 and P3 even higher than the SPM and ESPM. On the other hand, for the HE battery, the RMSEs are similar between the discharge and relaxation regions. If only the simulation accuracy is considered, then from all simplifications the DFN model with P4 is the model of choice for both a HE and HP battery.

Fig. 7 shows the RMSE and MSS among all simplifications and C-rates for the HE (Fig. 7a-c) and the HP (Fig. 7d-f) battery simulations. The RMSE in Fig. 7 is the one for the full simulation, i.e., combined CC-discharge and relaxation parts. The SPM, including all its approximations (SPM group), shows the highest MSS, averaging 98% for the HE battery and 96% for the HP battery and is therefore the best approach in terms of calculation speed. However, the simulation accuracy with the SPM group is poor and increases as a function of C-rate, as already concluded from Fig. 6. This especially holds for the HE battery. The

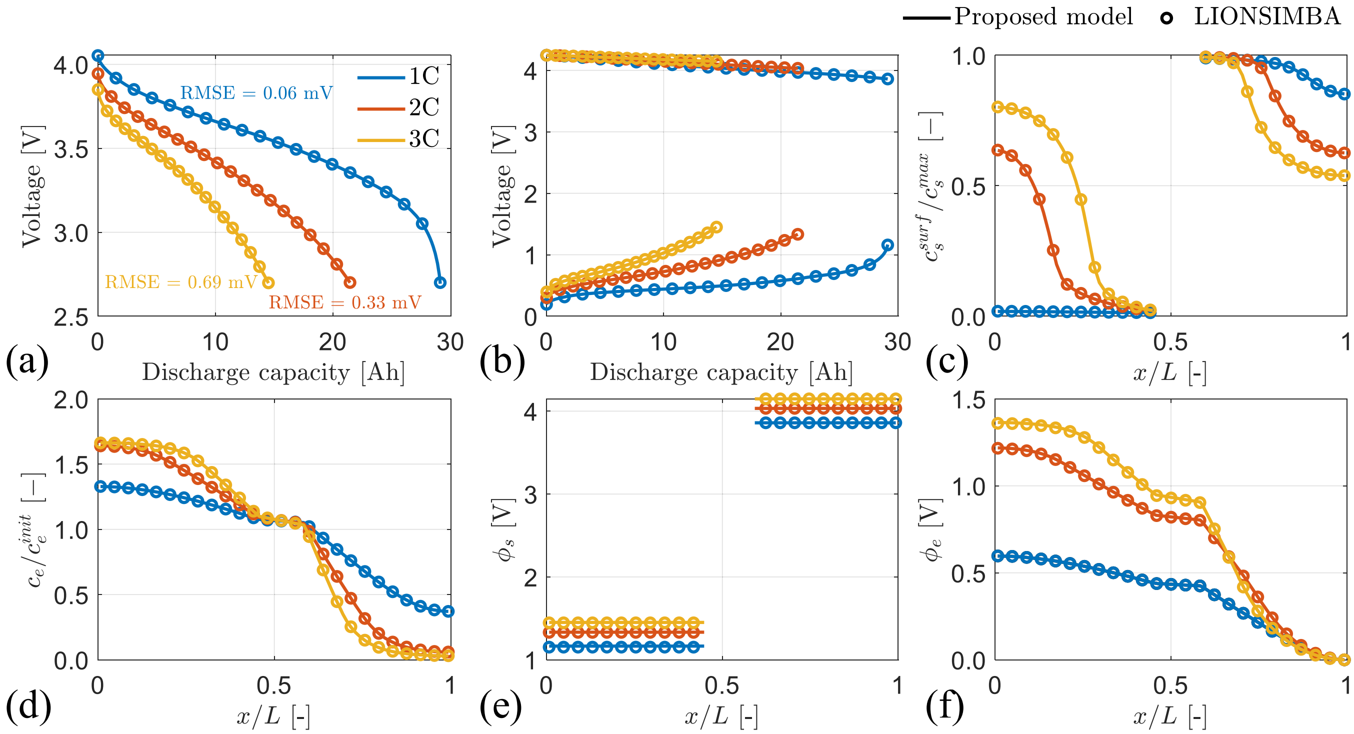

Fig. 4. Simulation results of the reference DFN model (solid lines) and LIONSIMBA toolbox (symbols) [41] for three C-rates (1, 2, 3C). Battery voltage (a), positive and negative electrode voltage (b), solid phase lithium concentration (c), electrolyte phase lithium concentration (d), solid phase potential (e) and electrolyte phase potential (f). The states in (c)-(f) are shown for the end of discharge.

average RMSE is, in this case, found to be 39 mV. In contrast, with an average of 27 mV the RMSE for the HP battery turns out to be somewhat lower, making the SPM potentially suitable for C-rate simulations not higher than 1C. From the SPM group it can be further concluded that the various approximations on top of the SPM with FDM do not lead to any significant gains in accuracy and simulation speed. For that reason, all SPM group (+ symbols) are overlapping. For the HP battery, the FDM leads to slightly better accuracies, but if neglecting this small difference, the method which is easiest to implement from a programming point of view can best be adopted.

The ESPM group (O symbols), including all approximations, shows a slightly lower MSS in comparison to the SPM group, averaging 96% and 94% for the HE and HP batteries, respectively. Because electrolyte dynamics are present, the ESPM outperforms the SPM with lower RMSE values and maintains fair accuracy (< 15 mV) until intermediate C-rates for the HE battery and for all C-rates for the HP battery. At the same time, the ESPM is not much inferior to the SPM when it comes to simulation speed, making the ESPM a favorable option for battery simulations, especially for real-time BMS applications. For the HE battery, the various approximations on top of the ESPM with FDM reveal no significant change in accuracy and simulation speed. However, among the ESPM group, noticeable accuracy differences are found for the HP battery, although the simulation speeds remain relatively unaffected. The preferred option is therefore using the FDM in combination with the ESPM.

When analyzing the DFN group (✳ symbols), the various approximations have a significant influence on simulation accuracy and speed. When it comes to simulation speed, the DFN group is far slower in comparison to the SPM and ESPM groups. On the other hand, the simulation accuracy of the DFN group is generally more favorable with respect to the SPM and ESPM groups. This is due to the capability of simulating the concentration distribution across each electrode with multiple particles, as opposed to just one particle. However, when comparing the accuracy of the DFN group between the HE and HP batteries, the accuracy for the HE battery simulations is generally better, which is the other way around for the SPM and ESPM groups. One of the reasons for lower accuracy for the HP battery can be attributed to the fact that higher C-rates are used for the HP battery in comparison to the HE battery. For example, when comparing the DFN-group-accuracies for a 1C-rate for the HE and HP battery (Fig. 7c and d), the accuracies are very similar. Increasing C-rates subsequently lead to lower accuracies.

Within the DFN group, the TPA method leads to the fastest simulation speed, obtaining an average MSS of 30% and 27% for the HE and HP batteries, respectively. However, the TPA also has the highest RMSE compared to the other approximations. For the HE battery, the accuracy of the TPA method in combination with the DFN model is relatively similar to the ESPM method, but for the HP battery, the ESPM method outperforms the DFN model with TPA with most of its approximations and is, therefore, more favorable for HP batteries. The DFN model with HPA shows a lower MSS than the DFN model with TPA. Average MSS values of 27 and 24% for the HE and HP batteries are obtained, respectively. The HPA method achieves a relatively low RMSE across the entire C-rate range for both batteries and outperforms the SPM and ESPM groups. The DFN model with P2, P3 and P4 approximations shows for both batteries and all C-rates the lowest MSS of all simplifications. The average MSS for P2 is around 23% for the HE battery and 13% for the HP battery. Although the MSS for P2 – P4 is practically the same, the accuracy considerably increases with approximation order for both batteries and all C-rates. When using Padé approximation, it’s therefore advised to always use the highest order (P4 in this study). It also can be concluded that the MSS for the HP battery is generally lower than that of the HE battery due to the battery properties, resulting in fewer nodes for the grids for the HP battery.

4.2.2. *Dynamic cycle results*

Fig. 8 shows a general overview of WLTP drive-cycle simulation results from the reference model and a selection of simplifications for both the HE (Fig. 8a-b) and HP (Fig. 8c-d) batteries. As explained in Section 3.2.2, mean discharge C-rates of 0.27 and 0.5C for the HE battery and 0.54 and 1C for the HP battery have been simulated. From the difference

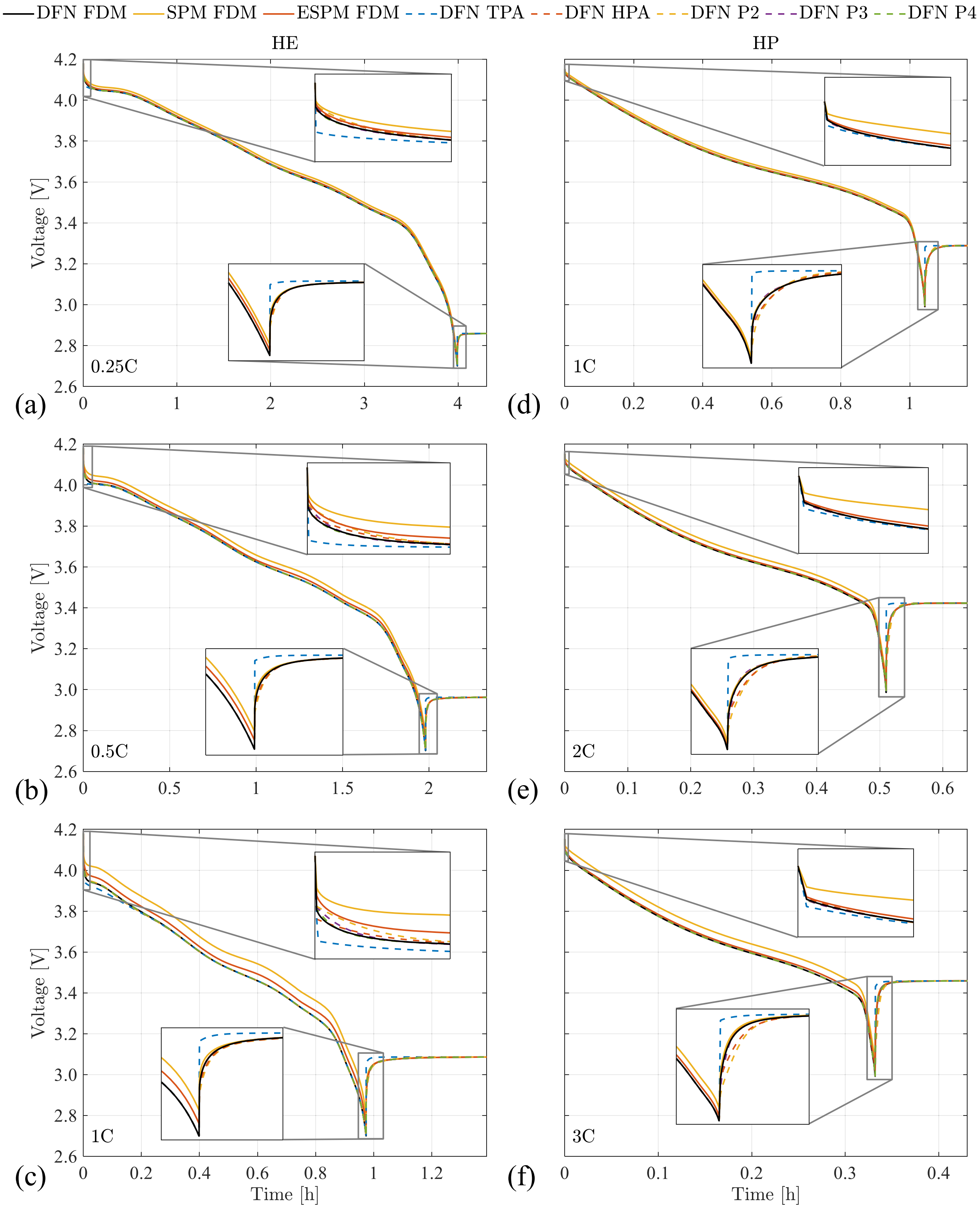

Fig. 5. Comparison of simulated voltage discharge curves between the reference DFN model and selected simplifications for both HE (a)-(c) and HP (d)-(f) batteries across different C-rates during CC-discharging and relaxation.

between the HE and HP simulation results, it can be observed that the HE battery shows larger voltage dynamics compared to the HP battery. This difference can be attributed to the difference in overpotentials between both batteries. The overpotential, which is a function of internal battery resistances, is lower for the HP battery in comparison to the HE battery.

As illustrated in Fig. 3, the WLTP cycle is divided into four regions (A1 – A4). In Fig. 8, these four regions are also indicated. For the HE battery, the first two regions with lower C-rates show similar results among all simplifications compared to the reference model. However, certain simplifications, particularly the SPM and TPA, show relatively high discrepancies in the A3-region and are becoming even more apparent in the A4-region, where the C-rates are highest. The ESPM has poor accuracy in the A4-region for the HE battery at a 0.5C mean discharge rate. These simulation differences are especially visible in the figure insets. On the other hand, for the HP battery, all simplifications

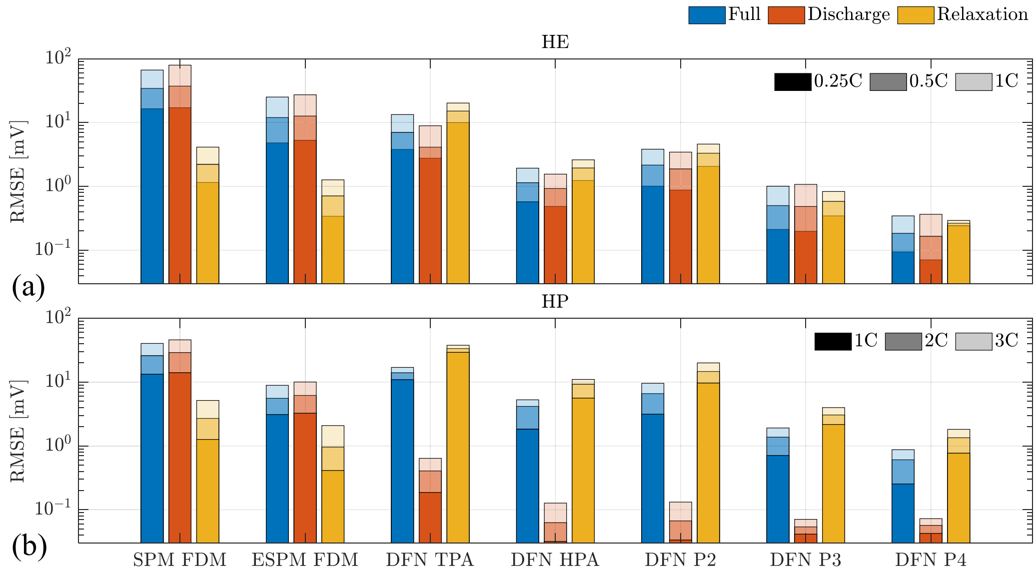

Fig. 6. RMSE between the reference model and a selection of simplifications using the full simulation (blue), discharge region (orange) and relaxation region (yellow) for the HE (a) and HP (b) battery. The different shades in the figure correspond to the C-rates indicated in the legend.

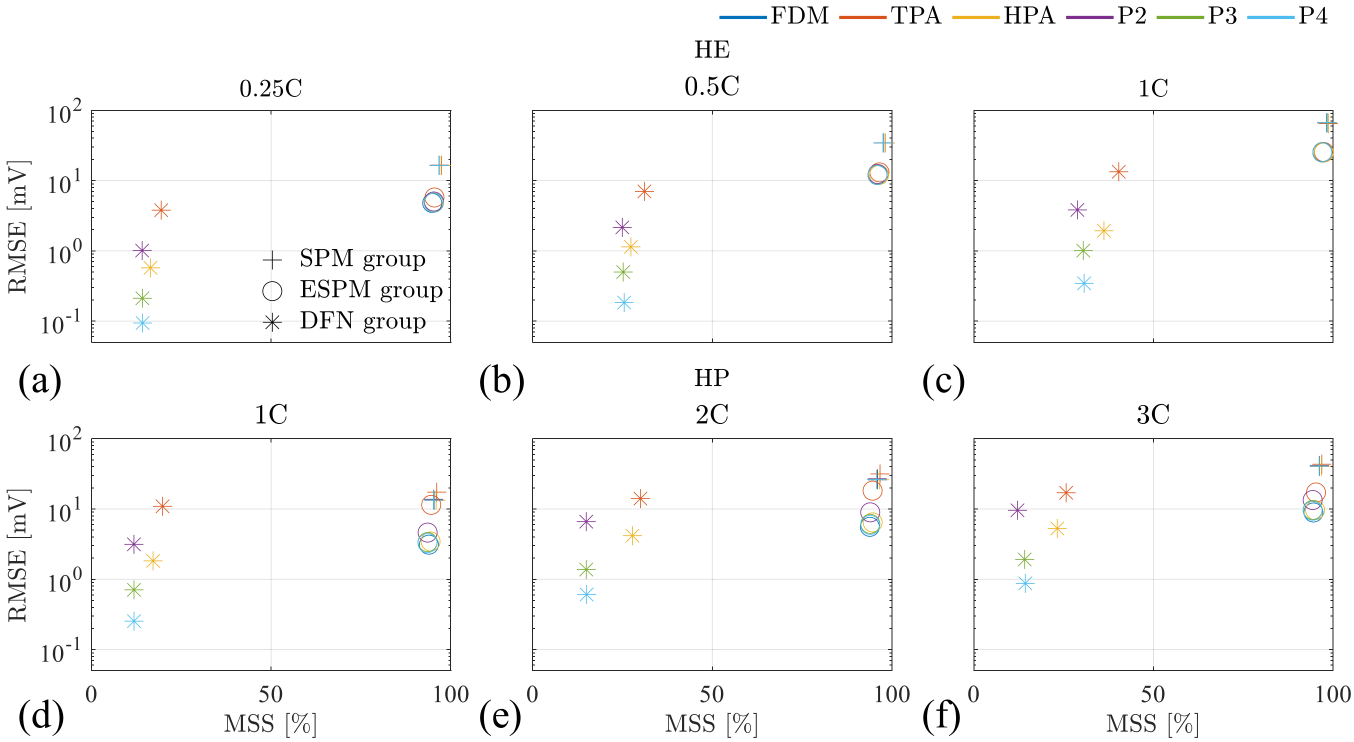

Fig. 7. RMSE and MSS comparison at various C-rates for a HE (a)-(c) and a HP (d)-(f) battery. The total RMSE and MSS are calculated on both the CC-discharge and relaxation parts and are with respect to the reference model in combination with the FDM approach.

demonstrate a good agreement with the reference model, except for the SPM model, particularly in the last two regions of the WLTP cycle, which is visually amplified in the figure insets and is further illustrated over time in the error figure, shown in supplementary Fig. S5. This indicates that electrolyte dynamics, which are present in all simplifications except in the SPM, have a significant importance at higher C-rates and should not be neglected for accurate simulations. Furthermore, the models with HPA and Padé approximations are all in good agreement with the reference model, even at high C-rates. Therefore, the HPA, P3 and P4 would be the preferred models to apply for a dynamic cycle such as the WLTP cycle. However, this is a conclusion without considering simulation speed. The figure insets in Fig. 8 clearly show that all models have less overpotential than the reference model. Such underestimation can likely be attributed to the characteristics of ROMs and approximations, which tend to disregard the nonlinear electrochemical behavior occurring in the battery. Consequently, this discrepancy in modeling accuracy tends to amplify as the C-rate increases. These tendencies toward underestimation compromises the ability of ROMs to be used for e. g. fast charging profiles, as they may fail to predict lithium-plating. This underscores the importance of considering internal variables in battery modeling to mitigate inaccuracies and ensure more reliable predictions.

The RMSE and MSS also have been calculated for the WLTP cycle and

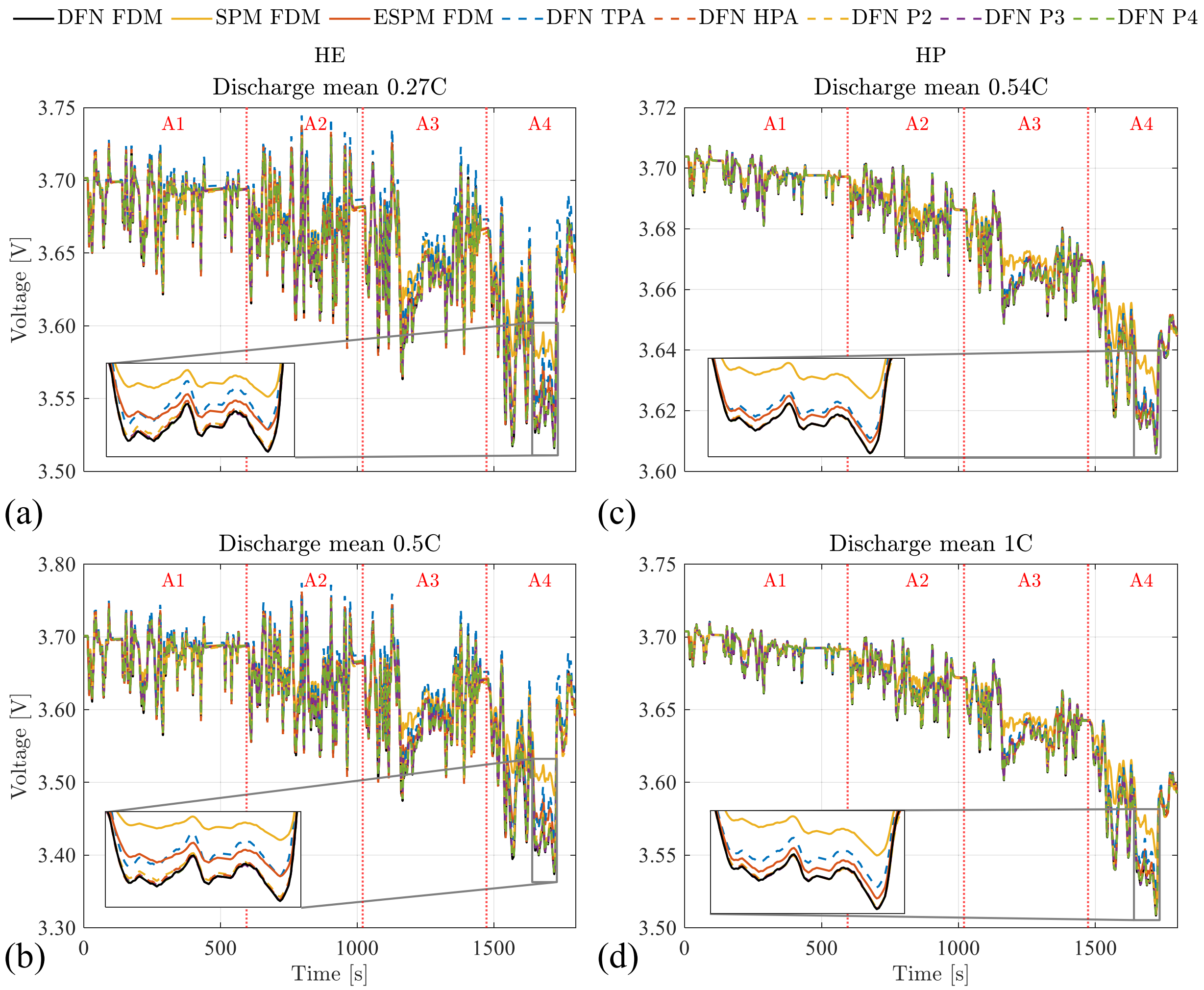

Fig. 8. Comparison of the simulated voltage between the reference model and a selection of simplifications for a HE (a)-(b) and HP (c)-(d) battery under various C-rates during application of the WLTP cycle. The insets show a magnification of a part of the A4-region between 1640 and 1750 s of the WLTP cycle.

are shown in Fig. 9 for a HE battery at C-rates of 0.27 and 0.5C, as well as the HP battery at 0.54 and 1C. The SPM group (+ symbols) shows a relatively high overall RMSE for the HE battery, averaging 16 mV for a mean discharge C-rate of 0.27C and 33 mV for the 0.5C-rate. The calculated maximum errors for 0.27C and 0.50C are 63 mV and 118 mV, respectively. Nonetheless, for the simulations on the HP battery with the SPM group, the RMSE is reduced to 7 mV at 0.54C and 14 mV at 1C. However, the maximum errors remain relatively high, exceeding 23 mV and 45 mV for 0.54C and 1C, respectively. Despite the high MSS for the SPM group, averaging around 97%, the SPM is not suitable for simulating the WLTP cycle for an HE battery due to it's relatively large RMSEs. As with the CC-discharge simulations, the various approximations on top of the SPM do not give significant changes in RMSE and MSS, making those redundant in combination with the SPM.

The ESPM group (O symbols) shows a good performance for both batteries, with an average RMSE of approximately 6 mV at 0.27C and 14 mV at 0.5C for the HE battery. Similarly, the RMSE for the HP battery is 1 mV at 0.54C and 2 mV at 1C. There is a noticeable improvement in terms of maximum errors when compared to the SPM group, with values of 32 mV at 0.27C and 59 mV at 0.5C for the HE battery and 4 mV at 0.54C and 10 mV at 1C for the HP battery. The ESPM also offers a fast simulation speed compared to the reference DFN model, with an average MSS of 96% and 94% for the HE and HP batteries, respectively. When evaluating the various approximations in combination with the ESPM, then it can be seen that the approximations only lead to RMSE changes in the case of simulating a HE battery. Moreover, in terms of simulation speed, the approximations on top of the ESPM have a neglectable effect. The TPA method shows the highest error in comparison to the other methods. From the HPA, P3 and P4 approximations similar results with relatively high accuracy can be obtained, while the simulation speeds are also similar. Given the relatively low RMSE and high MSS, the ESPM with either FDM, HPA, P3 or P4 approximations is therefore advised.

When analyzing the DFN group (✳ symbols), it immediately can be seen that simulation speeds are far slower with respect to the SPM and ESPM groups, as also concluded from the CC-discharge simulations in Section 4.2.1. Focusing on the HE battery in Fig. 9a and c, the TPA and HPA approximations show the highest MSS of all approximations for the DFN group. However, the TPA method underperforms when it comes to RMSE, which is similar to that of the ESPM group. This demonstrates that TPA is not suitable for fast load changes such as in dynamic cycles, resulting in lower accuracies and, therefore, a higher order model would be of advantage. The Padé approximations have a relatively low MSS, indicating simulation speeds similar to the reference model. As expected, the RMSE for P4 approximation is the lowest and is able to capture the dynamic processes in the battery. For the HP battery simulations (Fig. 9b and d), an interesting phenomenon is visible in the MSS of the approximations on the DFN group. Due to the relatively low number nodes in the electrodes (Section 3.3) for the HP battery in comparison to the HE battery, the approximations on top of the DFN model result in low simulation speed improvement with respect to the reference model. When the number of nodes is low, approximations have less influence on computational speed. Therefore, using

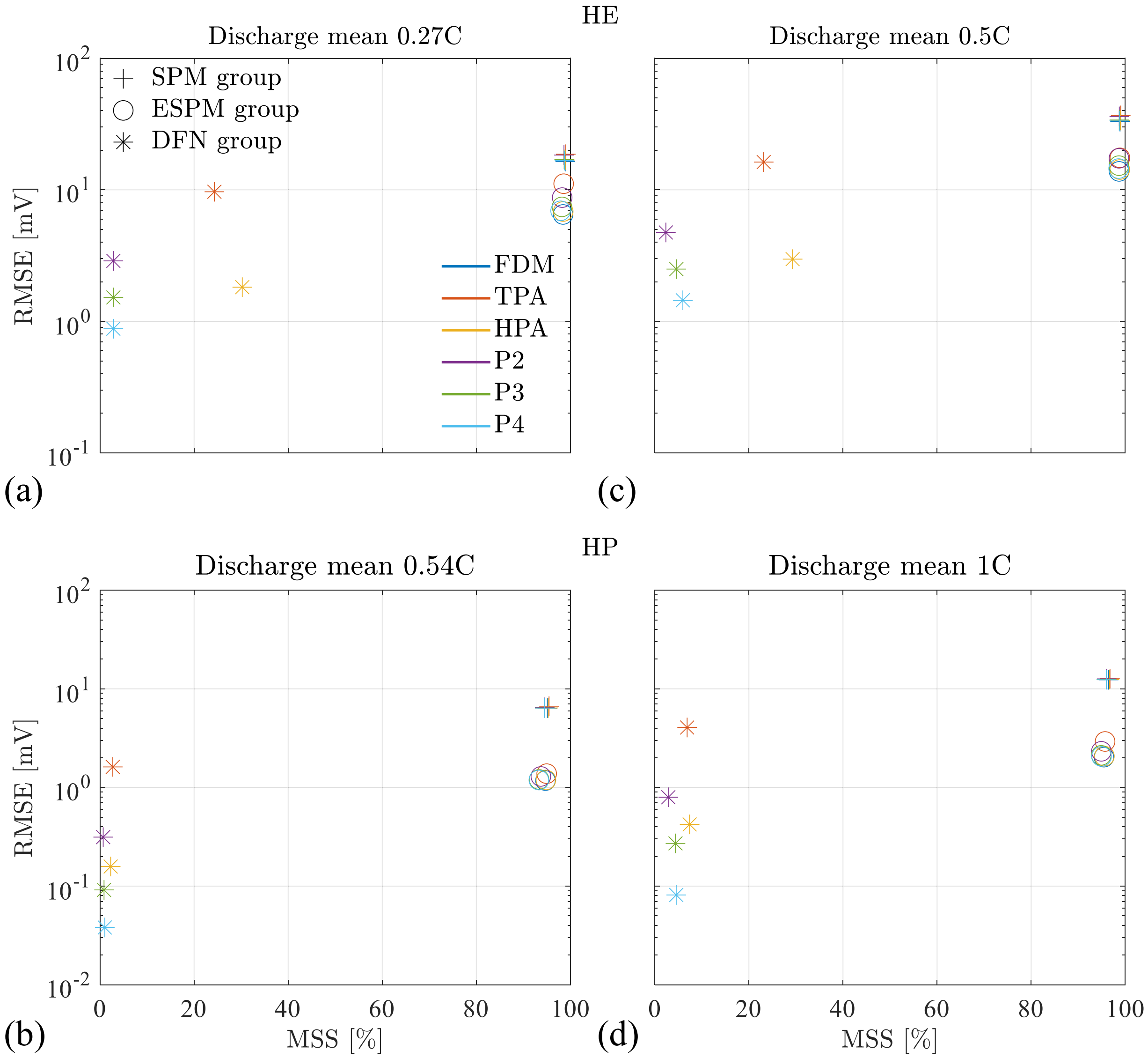

Fig. 9. RMSE and MSS comparison for all simplifications under simulation of the WLTP cycle for a HE (a)-(b) and HP (c)-(d) battery. The RMSE and MSS are calculated with respect to the reference DFN-model.

approximations with a low number of nodes is not recommended. An average MSS of 1.5% for the 0.54C-rate and 5.2% at 1C are found.

4.2.3. Summary of simulation results

Table 9 shows a general model performance overview which is based on the simulation results. The various simplified models are shown in the left column, the mean simulation speed in the right column and the accuracy for the different use cases in-between. Note that the simulation speed is the mean value of the selected simulations in this study. The legend displays the four RMSE boundaries, which are categorized as excellent (A, green), good (B, yellow), fair (C, orange), and poor (D, red). For the MSS, the boundaries range from 1 to 4, corresponding to ratings from excellent (1) to poor (4). Table S1 lists the detailed RMSEs and MSS results for all ROMs and approximations.

It can be concluded that the SPM has excellent calculation speed (97% MSS) with respect to the reference model. However, the SPM achieves poor accuracy (<15 mV RMSE) for simulating HE batteries under almost all conditions. The SPM accuracy slightly improves when simulating HP batteries at low C-rates for some operating conditions. On the other hand, the ESPM shows promising performance. The ESPM is simple and computationally excellent (≥96% MSS) compared to the reference model and performs good to fair up to intermediate C-rates for HE batteries and high C-rates for HP batteries. For dynamic cycle simulations on HP batteries, the ESPM performs excellent in terms of accuracy and good and fair under normal and scaled C-rates for HE batteries.

The approximation methods within the DFN group, specifically TPA and HPA, yield satisfactory results in terms of simulation speed. However, it's worth noting that the models employing TPA reveal the highest errors across various use cases, followed by P2 and HPA. Overall, the DFN model using P3 and P4 approximations prove to be the most accurate options. However, the simulation speeds are classified as poor.

In general, there is no single solution that offers an ideal trade-off between accuracy, simulation speed and simplicity. The choice of a model should be evaluated based on the expected operating conditions such as temperature, C-rate, battery type and required simulation speed. Fig. 10 shows a flow diagram as a guide for selecting model simplifications, in which the various steps are shown on how to find the appropriate model. It is important to note that the flow diagram is intended solely for selecting the appropriate simplification. If simulation speed is not a primary consideration, then the reference model can be used. However, for BMS applications, generating training data sets or

Table 9
Performance overview of a selection of simplifications with respect to the reference DFN model for CC-discharging plus relaxation and a WLTP cycle at various C-rates for a HE and HP battery.

Model	CC-discharge + relaxation						Dynamic cycle				Mean MSS
	Accuracy (Low C-rate) $I_{\mathrm{app}} = 0.25C$ (HE) $I_{\mathrm{app}} = 1.00C$ (HP)		Accuracy (Intermediate C-rate) $I_{\mathrm{app}} = 0.5C$ (HE) $I_{\mathrm{app}} = 2.0C$ (HP)		Accuracy (High C-rate) $I_{\mathrm{app}} = 1C$ (HE) $I_{\mathrm{app}} = 3C$ (HP)		Accuracy (Normal) $I_{\mathrm{app,mean}} \sim 0.27C$ (HE) $I_{\mathrm{app,mean}} \sim 0.54C$ (HP)		Accuracy (Scaled) $I_{\mathrm{app,mean}} \sim 0.5C$ (HE) $I_{\mathrm{app,mean}} \sim 1.0C$ (HP)		
Cell Type	HE	HP	HE	HP	HE	HP	HE	HP	HE	HP	All
DFN FDM						Reference model					
SPM FDM	D	C	D	D	D	D	D	B	D	C	1
ESPM FDM	B	B	C	B	D	B	B	B	C	B	1
DFN TPA	B	C	B	C	C	D	C	B	D	B	3
DFN HPA	A	B	B	B	B	B	B	A	B	A	3
DFN P2	A	B	B	B	B	C	B	A	B	A	4
DFN P3	A	A	A	B	A	B	B	A	B	A	4
DFN P4	A	A	A	A	A	A	A	A	B	A	4
	Boundaries RMSE [mV]		≤ 1	A	≤ 8	B	≤ 15	C	> 15	D	
	MSS [%]		≥ 80	1	≥ 50	2	≥ 20	3	< 20	4	

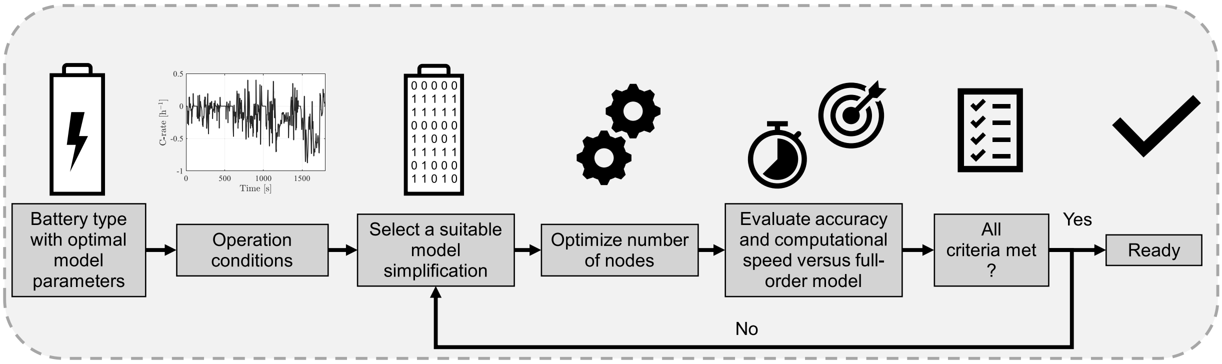

Fig. 10. Flow diagram as a guide for selecting model simplifications.

performing long-duration aging simulations, simulation speed is often a crucial factor, for which selecting the correct simplification becomes important.

4.3. Sensitivity analysis results

In the performed sensitivity analysis, the reference DFN model and both ROMs (ESPM and SPM) have been investigated. The ROMs neglect model features and are reduced in the number of parameters with respect to the DFN model, which could potentially lead to different parameter sensitivity. Fig. 11 shows the sensitivity analysis results, in which the sensitivity is classified in high ($\geq 1 \times 10^{-2}$), medium ($\geq 1 \times 10^{-4}$) and low ($< 1 \times 10^{-4}$). In Fig. 11a, b and c the DFN model parameters (25), the ESPM parameters (23) and SPM parameters (13) are shown, respectively. The sensitivity analysis reveals variations in parameter ranking and sensitivity among the three different models. For example, all geometric parameters for the solid electrodes, and partially transport, kinetics and concentration parameters were found to be highly sensitive for the DFN model. However, the level of sensitivity can vary depending on the model, as seen with parameters such as $R_{\mathrm{s,p}}$ and $k_{0,\mathrm{n}}$. $R_{\mathrm{s,p}}$ is highly sensitive for the DFN model and SPM, but medium sensitive for the ESPM. On the other hand, $k_{0,\mathrm{n}}$ is a highly sensitive parameter for the DFN model, but medium sensitive for both the SPM and ESPM.

The adoption of the same parameter values from the DFN model into both ROMs is feasible in some operation conditions since most of the highly sensitive parameters from the DFN model are also implemented into the ROMs, as shown in Fig. 11. This is evident when comparing simulations of discharges with relaxation and dynamic cycles at various C-rates for different battery types (Section 4.2). However, it is worth noting that when dealing with higher C-rates, the parameters for the ROMs may need to be re-estimated to maintain good accuracy. Therefore, caution is advised when applying these parameters to various

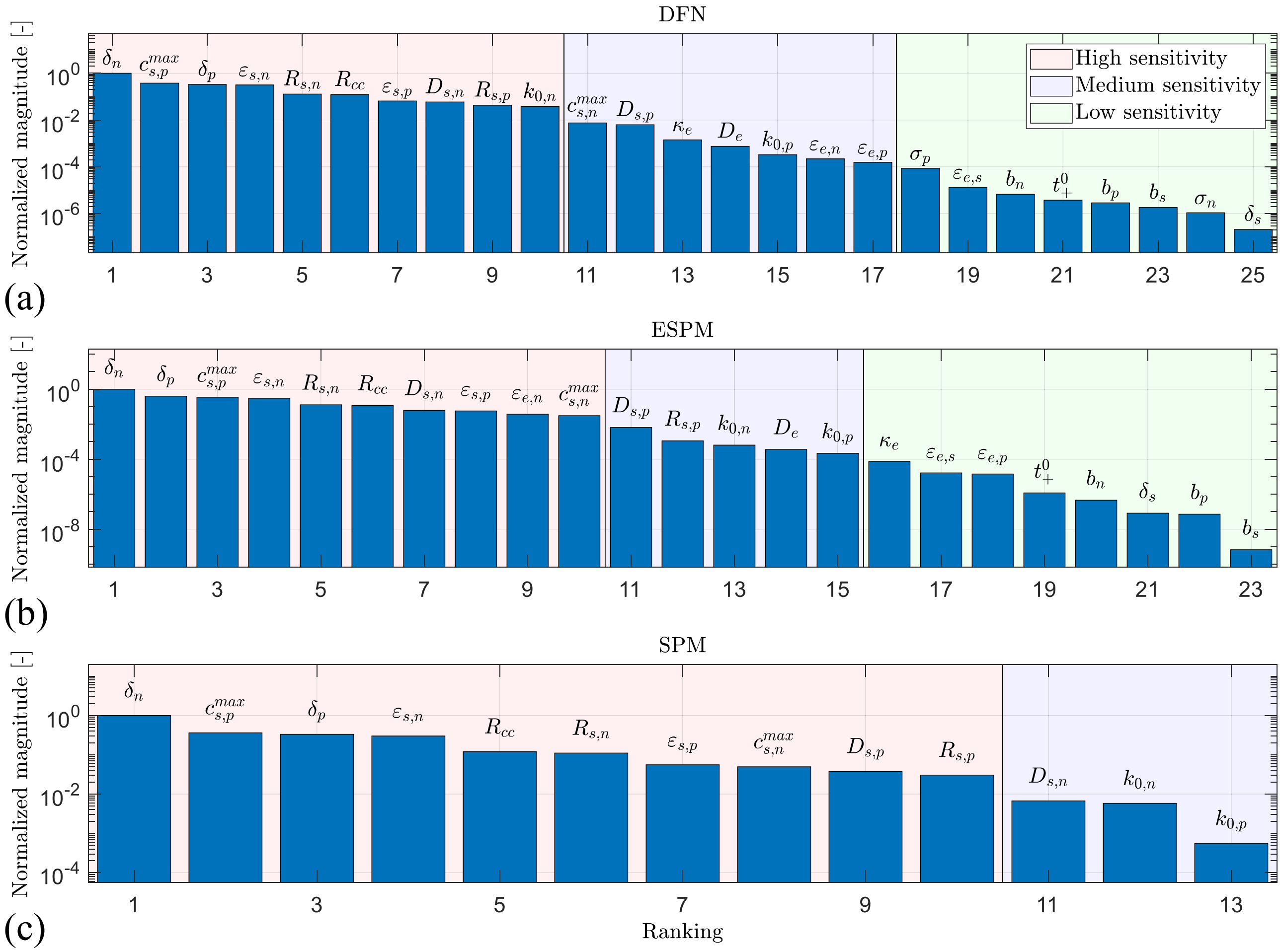

Fig. 11. Parameter sensitivity for the DFN (a), ESPM (b) and SPM (c). Sensitivity levels were categorized as high, medium and low, based on magnitude normalization: $\geq 1 \times 10^{-2}$ (high), $\geq 1 \times 10^{-4}$ (medium) and $< 1 \times 10^{-4}$ (low).

operating conditions, as this could potentially result in overfitting, meaning that model performance is good under one condition, but inferior under deviating conditions. ROMs might not fully capture certain phenomena or dynamics that can have a significant impact on model behavior under specific conditions. Hence, it is important to carefully assess the applicability of ROMs and consider the specific context in which they are used. Furthermore, adopting the same parameter values from ROMs into DFN models is not feasible because DFN models typically require a more extensive set of parameters than ROMs.

5. Conclusions

This study undertakes a thorough analysis of model simplifications for the DFN model in LIBs. The research encompasses an evaluation of ROMs, including the SPM and ESPM, as well as various approximations for simulating the solid phase lithium concentration. A comparison of these simplifications against the adopted reference DFN model is carried out across a range of operating conditions and battery types. Sensitivity analyses are also performed to explore the behavior of model parameters.

Simulation results demonstrate that ROMs offer advantages in terms of speed. The SPM, although fast in simulation time, tends to compromise on accuracy. In contrast, the ESPM significantly enhances accuracy, making it suitable for use at intermediate C-rates in HE batteries and even at high C-rates in HP batteries, with commendable accuracy under CC-discharge, relaxation, and dynamic conditions. The improvement of the SPM versus the ESPM underlines the importance of considering electrolyte dynamics. Combining the DFN model with different approximations enhances simulation speed, with improvements of up to 40% in computational efficiency. However, the accuracy of these simulations varies with the type and approximation order. Higher-order approximations lead to better accuracy but may come at the expense of computational efficiency. The DFN model in combination with HPA strikes a favorable balance between accuracy and speed under most conditions, whereas the DFN model with P4 yields the highest level of accuracy among the approximations. Polynomial approximations typically outperform Padé approximations in terms of simulation speed but is the other way around when it comes to accuracy with P3 or higher. Additionally, the sensitivity of model parameters plays a pivotal role in selecting the appropriate model, influencing the level of accuracy achieved.

The simulation results and comparisons illuminate the trade-offs between simulation speed and accuracy for two battery types and operating conditions. Each simplification method exhibits it's own set of advantages and disadvantages, allowing for a selection based on specific requirements. It is crucial to carefully consider the choice of model and simplifications based on the specific battery type and operating conditions, ensuring accurate capture of system dynamics and desired computational efficiency.

CRediT authorship contribution statement

Haider Adel Ali Ali: Writing – review & editing, Writing – original draft, Visualization, Validation, Software, Methodology, Investigation, Formal analysis, Data curation, Conceptualization. **Luc H.J.**

Raijmakers: . **Kudakwashe Chayambuka:** Writing – review & editing, Supervision. **Dmitri L. Danilov:** . **Peter H.L. Notten:** Writing – review & editing, Validation, Supervision. **Rüdiger-A. Eichel:** Resources, Funding acquisition.

Declaration of competing interest

The authors declare that they have no known competing financial interests or personal relationships that could have appeared to influence the work reported in this paper.

Data availability

Data will be made available on request.

Acknowledgement

The authors thank their colleagues at Forschungszentrum Jülich GmbH for their great support. This study has been developed in the LLEC::VxG and ALIBES projects, which are funded by the German Federal Ministry of Education and Research under Grant No. 03SF0628 and 13XP0530B, respectively.

Supplementary materials

Supplementary material associated with this article can be found, in the online version, at doi:10.1016/j.electacta.2024.144360.

References

[1] A. Masias, J. Marcicki, W.A. Paxton, Opportunities and challenges of lithium ion batteries in automotive applications, ACS Energy Lett. 6 (2021) 621–630, https://doi.org/10.1021/acsenergylett.0c02584.

[2] T. Chen, Y. Jin, H. Lv, A. Yang, M. Liu, B. Chen, Y. Xie, Q. Chen, Applications of lithium-ion batteries in grid-scale energy storage systems, Trans. Tianjin Univ. 26 (2020) 208–217, https://doi.org/10.1007/s12209-020-00236-w.

[3] R. Xiong, F. Sun, H. He, T.D. Nguyen, A data-driven adaptive state of charge and power capability joint estimator of lithium-ion polymer battery used in electric vehicles, Energy 63 (2013) 295–308, https://doi.org/10.1016/j.energy.2013.10.027.

[4] Y. Kang, B. Duan, Z. Zhou, Y. Shang, C. Zhang, A multi-fault diagnostic method based on an interleaved voltage measurement topology for series connected battery packs, J. Power. Sources. 417 (2019) 132–144, https://doi.org/10.1016/j.jpowsour.2019.01.058.

[5] H. Fang, Y. Wang, Z. Sahinoglu, T. Wada, S. Hara, State of charge estimation for lithium-ion batteries: an adaptive approach, Control Eng Pract 25 (2014) 45–54, https://doi.org/10.1016/j.conengprac.2013.12.006.

[6] Q. Lin, J. Wang, R. Xiong, W. Shen, H. He, Towards a smarter battery management system: a critical review on optimal charging methods of lithium ion batteries, Energy 183 (2019) 220–234, https://doi.org/10.1016/j.energy.2019.06.128.

[7] M.K. Tran, M. Mathew, S. Janhunen, S. Panchal, K. Raahemifar, R. Fraser, M. Fowler, A comprehensive equivalent circuit model for lithium-ion batteries, incorporating the effects of state of health, state of charge, and temperature on model parameters, J. Energy Storage 43 (2021) 103252, https://doi.org/10.1016/j.est.2021.103252.

[8] H. Rahimi-Eichi, U. Ojha, F. Baronti, M.-Y. Chow, Battery management system: an overview of its application in the smart grid and electric vehicles, IEEE Indus. Electron. Magaz. 7 (2013) 4–16, https://doi.org/10.1109/MIE.2013.2250351.

[9] K.A. Severson, P.M. Attia, N. Jin, N. Perkins, B. Jiang, Z. Yang, M.H. Chen, M. Aykol, P.K. Herring, D. Fraggedakis, M.Z. Bazant, S.J. Harris, W.C. Chueh, R. D. Braatz, Data-driven prediction of battery cycle life before capacity degradation, Nat. Energy 4 (2019) 383–391, https://doi.org/10.1038/s41560-019-0356-8.

[10] Z. Cui, L. Wang, Q. Li, K. Wang, A comprehensive review on the state of charge estimation for lithium-ion battery based on neural network, Int. J. Energy Res. 46 (2022) 5423–5440, https://doi.org/10.1002/er.7545.

[11] L. Xu, J. Wang, Q. Chen, Kalman filtering state of charge estimation for battery management system based on a stochastic fuzzy neural network battery model, Energy Convers. Manage 53 (2012) 33–39, https://doi.org/10.1016/j.enconman.2011.06.003.

[12] D. Yang, X. Zhang, R. Pan, Y. Wang, Z. Chen, A novel Gaussian process regression model for state-of-health estimation of lithium-ion battery using charging curve, J. Power. Sources. 384 (2018) 387–395, https://doi.org/10.1016/j.jpowsour.2018.03.015.

[13] Z. Deng, X. Hu, X. Lin, Y. Che, L. Xu, W. Guo, Data-driven state of charge estimation for lithium-ion battery packs based on Gaussian process regression, Energy 205 (2020) 118000, https://doi.org/10.1016/j.energy.2020.118000.

[14] D. Liu, J. Pang, J. Zhou, Y. Peng, M. Pecht, Prognostics for state of health estimation of lithium-ion batteries based on combination Gaussian process functional regression, Microelectron. Reliab. 53 (2013) 832–839, https://doi.org/10.1016/j.microrel.2013.03.010.

[15] M.A. Patil, P. Tagade, K.S. Hariharan, S.M. Kolake, T. Song, T. Yeo, S. Doo, A novel multistage support vector machine based approach for li ion battery remaining useful life estimation, Appl. Energy 159 (2015) 285–297, https://doi.org/10.1016/j.apenergy.2015.08.119.

[16] X. Feng, C. Weng, X. He, X. Han, L. Lu, D. Ren, M. Ouyang, Online state-of-health estimation for li-ion battery using partial charging segment based on support vector machine, IEEe Trans. Veh. Technol. 68 (2019) 8583–8592, https://doi.org/10.1109/TVT.2019.2927120.

[17] J.C. Álvarez Antón, P.J. García Nieto, C. Blanco Viejo, J.A. Vilán Vilán, Support vector machines used to estimate the battery state of charge, IEEe Trans. Power. Electron. 28 (2013) 5919–5926, https://doi.org/10.1109/TPEL.2013.2243918.

[18] G. You, S. Park, D. Oh, Real-time state-of-health estimation for electric vehicle batteries: a data-driven approach, Appl. Energy 176 (2016) 92–103, https://doi.org/10.1016/j.apenergy.2016.05.051.

[19] M. Ragone, V. Yurkiv, A. Ramasubramanian, B. Kashir, F. Mashayek, Data driven estimation of electric vehicle battery state-of-charge informed by automotive simulations and multi-physics modeling, J. Power. Sources. 483 (2021) 229108, https://doi.org/10.1016/j.jpowsour.2020.229108.

[20] O. Ahmadzadeh, Y. Wang, D. Soudbakhsh, A data-driven framework for learning governing equations of Li-ion batteries and co-estimating voltage and state-of-charge, J. Energy Storage 84 (2024) 110743, https://doi.org/10.1016/j.est.2024.110743.

[21] R. Li, S. O'Kane, J. Huang, M. Marinescu, G.J. Offer, A million cycles in a day: enabling high-throughput computing of lithium-ion battery degradation with physics-based models, J. Power. Sources. 598 (2024) 234184, https://doi.org/10.1016/j.jpowsour.2024.234184.

[22] Z. Chen, D.L. Danilov, R.-A. Eichel, P.H.L. Notten, Porous Electrode Modeling and its Applications to Li-Ion Batteries, Adv. Energy Mater. 12 (2022) 2201506, https://doi.org/10.1002/aenm.202201506.

[23] B. Yann Liaw, G. Nagasubramanian, R.G. Jungst, D.H. Doughty, Modeling of lithium ion cells—A simple equivalent-circuit model approach, Solid. State Ion. 175 (2004) 835–839, https://doi.org/10.1016/j.ssi.2004.09.049.

[24] T. Feng, L. Yang, X. Zhao, H. Zhang, J. Qiang, Online identification of lithium-ion battery parameters based on an improved equivalent-circuit model and its implementation on battery state-of-power prediction, J. Power. Sources. 281 (2015) 192–203, https://doi.org/10.1016/j.jpowsour.2015.01.154.

[25] H.J. Bergveld, W.S. Kruijt, P.H.L. Notten, H.J. Bergveld, W.S. Kruijt, P.H.L. Notten, Battery Management Systems. Battery Management Systems: Design by Modelling, Springer, Netherlands, Dordrecht, 2002, pp. 9–30, https://doi.org/10.1007/978-94-017-0843-2_2.

[26] J. Meng, G. Luo, M. Ricco, M. Swierczynski, D.-I. Stroe, R. Teodorescu, Overview of lithium-ion battery modeling methods for state-of-charge estimation in electrical vehicles, Applied Sciences 8 (2018) 659, https://doi.org/10.3390/app8050659.

[27] S. Nejad, D.T. Gladwin, D.A. Stone, A systematic review of lumped-parameter equivalent circuit models for real-time estimation of lithium-ion battery states, J. Power. Sources. 316 (2016) 183–196, https://doi.org/10.1016/j.jpowsour.2016.03.042.

[28] S. Pang, J. Farrell, J. Du, M. Barth, Battery state-of-charge estimation, in: Proceedings of the 2001 American Control Conference. (Cat. No.01CH37148) 2, 2001, pp. 1644–1649, https://doi.org/10.1109/ACC.2001.945964.

[29] J. Newman, W. Tiedemann, Porous-electrode theory with battery applications, AIChE Journal 21 (1975) 25–41, https://doi.org/10.1002/aic.690210103.

[30] C. Zou, A.G. Kallapur, C. Manzie, D. Nešić, PDE battery model simplification for SOC and SOH estimator design, in: Proceedings of the 54th IEEE Conference on Decision and Control (CDC), 2015, pp. 1328–1333, https://doi.org/10.1109/CDC.2015.7402395.

[31] R. Klein, N.A. Chaturvedi, J. Christensen, J. Ahmed, R. Findeisen, A. Kojic, Optimal charging strategies in lithium-ion battery, in: Proceedings of the 2011 American Control Conference, 2011, pp. 382–387, https://doi.org/10.1109/ACC.2011.5991497.

[32] J.V. Pastor, A. García, J. Monsalve-Serrano, D. Golke, Analysis of the aging effects on the thermal runaway characteristics of Lithium-Ion cells through stepwise reactions, Appl. Therm. Eng. 230 (2023) 120685, https://doi.org/10.1016/j.applthermaleng.2023.120685.

[33] T.G. Tranter, R. Timms, T.M.M. Heenan, S.G. Marquis, V. Sulzer, A. Jnawali, M.D. R. Kok, C.P. Please, S.J. Chapman, P.R. Shearing, D.J.L. Brett, Probing heterogeneity in li-ion batteries with coupled multiscale models of electrochemistry and thermal transport using tomographic domains, J. Electrochem. Soc. 167 (2020) 110538, https://doi.org/10.1149/1945-7111/aba44b.

[34] S. Vashisht, D. Rakshit, S. Panchal, M. Fowler, R. Fraser, Thermal behaviour of Li-ion battery: an improved electrothermal model considering the effects of depth of discharge and temperature, J. Energy Storage 70 (2023) 107797, https://doi.org/10.1016/j.est.2023.107797.

[35] C. Hong, H. Cho, D. Hong, S.-K. Oh, Y. Kim, An improved thermal single particle model and parameter estimation for high-capacity battery cell, Electrochim. Acta 439 (2023) 141638, https://doi.org/10.1016/j.electacta.2022.141638.

[36] K. Kumaresan, G. Sikha, R.E. White, Thermal model for a li-ion cell, J. Electrochem. Soc. 155 (2007) A164, https://doi.org/10.1149/1.2817888.

[37] M. Doyle, J. Newman, A.S. Gozdz, C.N. Schmutz, J.-M. Tarascon, Comparison of modeling predictions with experimental data from plastic lithium ion cells, J. Electrochem. Soc. 143 (1996) 1890, https://doi.org/10.1149/1.1836921.

[38] V. Ramadesigan, P.W.C. Northrop, S. De, S. Santhanagopalan, R.D. Braatz, V. R. Subramanian, Modeling and simulation of lithium-ion batteries from a systems engineering perspective, J. Electrochem. Soc. 159 (2012) R31, https://doi.org/10.1149/2.018203jes.

[39] J. Newman, N.P. Balsara, Electrochemical Systems, John Wiley & Sons, 2021.

[40] M. Doyle, T.F. Fuller, J. Newman, Modeling of galvanostatic charge and discharge of the lithium/polymer/insertion cell, J. Electrochem. Soc. 140 (1993) 1526, https://doi.org/10.1149/1.2221597.

[41] M. Torchio, L. Magni, R.B. Gopaluni, R.D. Braatz, D.M. Raimondo, LIONSIMBA: a matlab framework based on a finite volume model suitable for Li-Ion battery design, simulation, and control, J. Electrochem. Soc. 163 (2016) A1192–A1205, https://doi.org/10.1149/2.0291607jes.

[42] Z. Deng, L. Yang, H. Deng, Y. Cai, D. Li, Polynomial approximation pseudo-two-dimensional battery model for online application in embedded battery management system, Energy 142 (2018) 838–850, https://doi.org/10.1016/j.energy.2017.10.097.

[43] G. Fan, K. Pan, M. Canova, A comparison of model order reduction techniques for electrochemical characterization of Lithium-ion batteries, in: Proceedings of the 54th IEEE Conference on Decision and Control (CDC), IEEE, Osaka, 2015, pp. 3922–3931, https://doi.org/10.1109/CDC.2015.7402829.

[44] C.Y. Wang, W.B. Gu, B.Y. Liaw, Micro-macroscopic coupled modeling of batteries and fuel cells: I. Model development, J. Electrochem. Soc. 145 (1998) 3407, https://doi.org/10.1149/1.1838820.

[45] Z. Khalik, M.C.F. Donkers, H.J. Bergveld, Model simplifications and their impact on computational complexity for an electrochemistry-based battery modeling toolbox, J. Power. Sources. 488 (2021) 229427, https://doi.org/10.1016/j.jpowsour.2020.229427.

[46] V.R. Subramanian, V.D. Diwakar, D. Tapriyal, Efficient macro-micro scale coupled modeling of batteries, J. Electrochem. Soc. 152 (2005) A2002, https://doi.org/10.1149/1.2032427.

[47] X. Han, M. Ouyang, L. Lu, J. Li, Simplification of physics-based electrochemical model for lithium ion battery on electric vehicle. Part I: diffusion simplification and single particle model, J. Power. Sources. 278 (2015) 802–813, https://doi.org/10.1016/j.jpowsour.2014.12.101.

[48] N.T. Tran, M. Vilathgamuwa, T. Farrell, S.S. Choi, Y. Li, J. Teague, A Padé approximate model of lithium ion batteries, J. Electrochem. Soc. 165 (2018) A1409, https://doi.org/10.1149/2.0651807jes.

[49] Y. Shi, G. Prasad, Z. Shen, C.D. Rahn, Discretization methods for battery systems modeling, in: Proceedings of the American Control Conference, 2011, pp. 356–361, https://doi.org/10.1109/ACC.2011.5990857.

[50] J.C. Forman, S. Bashash, J.L. Stein, H.K. Fathy, Reduction of an electrochemistry-based li-ion battery model via quasi-linearization and padé approximation, J. Electrochem. Soc. 158 (2010) A93, https://doi.org/10.1149/1.3519059.

[51] W. Luo, C. Lyu, L. Wang, L. Zhang, A new extension of physics-based single particle model for higher charge–discharge rates, J. Power. Sources. 241 (2013) 295–310, https://doi.org/10.1016/j.jpowsour.2013.04.129.

[52] F. Brosa Planella, M. Sheikh, W.D. Widanage, Systematic derivation and validation of a reduced thermal-electrochemical model for lithium-ion batteries using asymptotic methods, Electrochim. Acta 388 (2021) 138524, https://doi.org/10.1016/j.electacta.2021.138524.

[53] W. Li, Y. Fan, F. Ringbeck, D. Jöst, X. Han, M. Ouyang, D.U. Sauer, Electrochemical model-based state estimation for lithium-ion batteries with adaptive unscented Kalman filter, J. Power. Sources. 476 (2020) 228534, https://doi.org/10.1016/j.jpowsour.2020.228534.

[54] S.G. Marquis, R. Timms, V. Sulzer, C.P. Please, S.J. Chapman, A suite of reduced-order models of a single-layer lithium-ion pouch cell, J. Electrochem. Soc. 167 (2020) 140513, https://doi.org/10.1149/1945-7111/abbce4.

[55] K.A. Smith, C.D. Rahn, C.Y. Wang, Control oriented 1D electrochemical model of lithium ion battery, Energy Convers. Manage 48 (2007) 2565–2578, https://doi.org/10.1016/j.enconman.2007.03.015.

[56] P. Ramadass, B. Haran, P.M. Gomadam, R. White, B.N. Popov, Development of first principles capacity fade model for Li-Ion cells, J. Electrochem. Soc. 151 (2004) A196, https://doi.org/10.1149/1.1634273.

[57] S. Khaleghi Rahimian, S. Rayman, R.E. White, Extension of physics-based single particle model for higher charge–discharge rates, J. Power. Sources. 224 (2013) 180–194, https://doi.org/10.1016/j.jpowsour.2012.09.084.

[58] S. Santhanagopalan, Q. Zhang, K. Kumaresan, R.E. White, Parameter estimation and life modeling of lithium-ion cells, J. Electrochem. Soc. 155 (2008) A345, https://doi.org/10.1149/1.2839630.

[59] V.R. Subramanian, V. Boovaragavan, V.D. Diwakar, Toward real-time simulation of physics based lithium-ion battery models, Electrochem. Solid State Lett. 10 (2007) A255, https://doi.org/10.1149/1.2776128.

[60] S.J. Moura, F.B. Argomedo, R. Klein, A. Mirtabatabaei, M. Krstic, Battery state estimation for a single particle model with electrolyte dynamics, IEEE Trans. Control Syst. Technol. 25 (2017) 453–468, https://doi.org/10.1109/TCST.2016.2571663.

[61] G. Richardson, I. Korotkin, R. Ranom, M. Castle, J.M. Foster, Generalised single particle models for high-rate operation of graded lithium-ion electrodes: systematic derivation and validation, Electrochim. Acta 339 (2020) 135862, https://doi.org/10.1016/j.electacta.2020.135862.

[62] P. Hashemzadeh, M. Désilets, M. Lacroix, A. Jokar, Investigation of the P2D and of the modified single-particle models for predicting the nonlinear behavior of Li-ion batteries, J. Energy Storage 52 (2022) 104909, https://doi.org/10.1016/j.est.2022.104909.

[63] F.B. Planella, W. Ai, A.M. Boyce, A. Ghosh, I. Korotkin, S. Sahu, V. Sulzer, R. Timms, T.G. Tranter, M. Zyskin, S.J. Cooper, J.S. Edge, J.M. Foster, M. Marinescu, B. Wu, G. Richardson, A continuum of physics-based lithium-ion battery models reviewed, Prog. Energy 4 (2022) 042003, https://doi.org/10.1088/2516-1083/ac7d31.

[64] K. Liu, Y. Gao, C. Zhu, K. Li, M. Fei, C. Peng, X. Zhang, Q.-L. Han, Electrochemical modeling and parameterization towards control-oriented management of lithium-ion batteries, Control Eng. Pract. 124 (2022) 105176, https://doi.org/10.1016/j.conengprac.2022.105176.

[65] Y. Li, D. Karunathilake, D.M. Vilathgamuwa, Y. Mishra, T.W. Farrell, S.S. Choi, C. Zou, Model order reduction techniques for physics-based lithium-ion battery management: a survey, IEEE Indus. Electron. Magaz. 16 (2022) 36–51, https://doi.org/10.1109/MIE.2021.3100318.

[66] J.Le Houx, D. Kramer, Physics based modelling of porous lithium ion battery electrodes—A review, Energy Reports 6 (2020) 1–9, https://doi.org/10.1016/j.egyr.2020.02.021.

[67] A. Jokar, B. Rajabloo, M. Désilets, M. Lacroix, Review of simplified Pseudo-two-Dimensional models of lithium-ion batteries, J. Power. Sources. 327 (2016) 44–55, https://doi.org/10.1016/j.jpowsour.2016.07.036.

[68] C.-H. Chen, F.B. Planella, K. O'Regan, D. Gastol, W.D. Widanage, E. Kendrick, Development of experimental techniques for parameterization of multi-scale lithium-ion battery models, J. Electrochem. Soc. 167 (2020) 080534, https://doi.org/10.1149/1945-7111/ab9050.

[69] N.T. Tran, M. Vilathgamuwa, T. Farrell, S.S. Choi, Matlab simulation of lithium ion cell using electrochemical single particle model, in: Proceedings of the IEEE 2nd Annual Southern Power Electronics Conference (SPEC), 2016, pp. 1–6, https://doi.org/10.1109/SPEC.2016.7846195.

[70] N.A. Chaturvedi, R. Klein, J. Christensen, J. Ahmed, A. Kojic, Algorithms for advanced battery-management systems, IEEE Control Systems Magazine 30 (2010) 49–68, https://doi.org/10.1109/MCS.2010.936293.

[71] J. Marcicki, M. Canova, A.T. Conlisk, G. Rizzoni, Design and parametrization analysis of a reduced-order electrochemical model of graphite/LiFePO4 cells for SOC/SOH estimation, J. Power. Sources. 237 (2013) 310–324, https://doi.org/10.1016/j.jpowsour.2012.12.120.

[72] Y. Zhao, S.-Y. Choe, Evaluation of Order Reduction Techniques for Porous Electrode Diffusion Equation in Lithium Ion Model, SAE International, Warrendale, PA, 2014, https://doi.org/10.4271/2014-01-1835.

[73] L. Xia, E. Najafi, Z. Li, H.J. Bergveld, M.C.F. Donkers, A computationally efficient implementation of a full and reduced-order electrochemistry-based model for Li-ion batteries, Appl. Energy 208 (2017) 1285–1296, https://doi.org/10.1016/j.apenergy.2017.09.025.

[74] J. Schmalstieg, C. Rahe, M. Ecker, D.U. Sauer, Full cell parameterization of a high-power lithium-ion battery for a physico-chemical model: part I. Physical and electrochemical parameters, J. Electrochem. Soc. 165 (2018) A3799, https://doi.org/10.1149/2.0321816jes.

[75] D. Tsokolis, S. Tsiakmakis, A. Dimaratos, G. Fontaras, P. Pistikopoulos, B. Ciuffo, Z. Samaras, Fuel consumption and CO2 emissions of passenger cars over the new worldwide harmonized test protocol, Appl. Energy 179 (2016) 1152–1165, https://doi.org/10.1016/j.apenergy.2016.07.091.

[76] Nissan Leaf e+, EV Database (n.d.). ev-database.org/car/1144/Nissan-Leaf-eplus (accessed April 21, 2023).

[77] the-slipperiest-car-on-the-road.pdf, (n.d.). www.tesla.com/sites/default/files/blog_attachments/the-slipperiest-car-on-the-road.pdf (accessed April 21, 2023).

[78] Nissan Leaf e+ 62 kWh - tech specs and prices | myEVreview, (n.d.). www.myevreview.com/tech-specs/nissan/leaf/e-62-kwh (accessed April 21, 2023).

[79] S. Bhoir, P. Caliandro, C. Brivio, Impact of V2G service provision on battery life, J. Energy Storage 44 (2021) 103178, https://doi.org/10.1016/j.est.2021.103178.

[80] B.F. Lund, B.A. Foss, Parameter ranking by orthogonalization—Applied to nonlinear mechanistic models, Automatica 44 (2008) 278–281, https://doi.org/10.1016/j.automatica.2007.04.006.

[81] M. Andersson, M. Streb, J.Y. Ko, V. Löfqvist Klass, M. Klett, H. Ekström, M. Johansson, G. Lindbergh, Parametrization of physics-based battery models from input–output data: a review of methodology and current research, J. Power. Sources. 521 (2022) 230859, https://doi.org/10.1016/j.jpowsour.2021.230859.

[82] Z. Khalik, M.C.F. Donkers, J. Sturm, H.J. Bergveld, Parameter estimation of the Doyle–Fuller–Newman model for Lithium-ion batteries by parameter normalization, grouping, and sensitivity analysis, J. Power. Sources. 499 (2021) 229901, https://doi.org/10.1016/j.jpowsour.2021.229901.

[83] N. Jin, D.L. Danilov, P.M.J. Van den Hof, M.c.f. Donkers, Parameter estimation of an electrochemistry-based lithium-ion battery model using a two-step procedure and a parameter sensitivity analysis, Int. J. Energy Res. 42 (2018) 2417–2430, https://doi.org/10.1002/er.4022.

[84] S.V. Erhard, P.J. Osswald, P. Keil, E. Höffer, M. Haug, A. Noel, J. Wilhelm, B. Rieger, K. Schmidt, S. Kosch, F.M. Kindermann, F. Spingler, H. Kloust, T. Thoennessen, A. Rheinfeld, A. Jossen, Simulation and measurement of the current density distribution in lithium-ion batteries by a multi-tab cell approach, J. Electrochem. Soc. 164 (2017) A6324–A6333, https://doi.org/10.1149/2.0551701jes.

[85] A. Rheinfeld, J. Sturm, A. Noel, J. Wilhelm, A. Kriston, A. Pfrang, A. Jossen, Quasi-isothermal external short circuit tests applied to lithium-ion cells: part II. Modeling and simulation, J. Electrochem. Soc. 166 (2019) A151, https://doi.org/10.1149/2.0071902jes.

[86] M. Ecker, T.K.D. Tran, P. Dechent, S. Käbitz, A. Warnecke, D.U. Sauer, Parameterization of a physico-chemical model of a lithium-ion battery: I. Determination of parameters, J. Electrochem. Soc. 162 (2015) A1836, https://doi.org/10.1149/2.0551509jes.

[87] Y. Ji, Y. Zhang, C.-Y. Wang, Li-Ion cell operation at low temperatures, J. Electrochem. Soc. 160 (2013) A636, https://doi.org/10.1149/2.047304jes.

[88] J. Mao, W. Tiedemann, J. Newman, Simulation of temperature rise in Li-ion cells at very high currents, J. Power. Sources. 271 (2014) 444–454, https://doi.org/10.1016/j.jpowsour.2014.08.033.

[89] A. Awarke, S. Pischinger, J. Ogrzewalla, Pseudo 3D modeling and analysis of the SEI growth distribution in large format Li-Ion polymer pouch cells, J. Electrochem. Soc. 160 (2012) A172, https://doi.org/10.1149/2.022302jes.

[90] H. Lundgren, M. Behm, G. Lindbergh, Electrochemical Characterization and Temperature Dependency of Mass-Transport Properties of LiPF6 in EC:DEC, J. Electrochem. Soc. 162 (2014) A413, https://doi.org/10.1149/2.0641503jes.

[91] A. Nyman, M. Behm, G. Lindbergh, Electrochemical characterisation and modelling of the mass transport phenomena in LiPF6–EC–EMC electrolyte, Electrochim. Acta 53 (2008) 6356–6365, https://doi.org/10.1016/j.electacta.2008.04.023.

[92] L.O. Valøen, J.N. Reimers, Transport properties of LiPF6-based Li-Ion battery electrolytes, J. Electrochem. Soc. 152 (2005) A882, https://doi.org/10.1149/1.1872737.

[93] L. Cai, R.E. White, Mathematical modeling of a lithium ion battery with thermal effects in COMSOL Inc. Multiphysics (MP) software, J. Power. Sources. 196 (2011) 5985–5989, https://doi.org/10.1016/j.jpowsour.2011.03.017.